

# BRNO UNIVERSITY OF TECHNOLOGY

VYSOKÉ UČENÍ TECHNICKÉ V BRNĚ

## FACULTY OF MECHANICAL ENGINEERING

FAKULTA STROJNÍHO INŽENÝRSTVÍ

## INSTITUTE OF PHYSICAL ENGINEERING

ÚSTAV FYZIKÁLNÍHO INŽENÝRSTVÍ

# OPTICAL DICHROISM IN VORTEX ELECTRON ENERGY-LOSS SPECTROSCOPY

OPTICKÝ DICHROISMUS VE SPEKTROSKOPII ENERGIOVÝCH ZTRÁT VORTEXOVÝCH ELEKTRONŮ

## BACHELOR'S THESIS

BAKALÁŘSKÁ PRÁCE

### AUTHOR

AUTOR PRÁCE

**Martin Ošmera**

### SUPERVISOR

VEDOUCÍ PRÁCE

**Ing. Andrea Konečná, Ph.D.**

**BRNO 2022**



# Assignment Bachelor's Thesis

Institut: Institute of Physical Engineering  
Student: **Martin Ošmera**  
Degree programm: Physical Engineering and Nanotechnology  
Branch: no specialisation  
Supervisor: **Ing. Andrea Konečná, Ph.D.**  
Academic year: 2021/22

As provided for by the Act No. 111/98 Coll. on higher education institutions and the BUT Study and Examination Regulations, the director of the Institute hereby assigns the following topic of Bachelor's Thesis:

## Optical dichroism in vortex electron energy–loss spectroscopy

### **Brief Description:**

Transmission electron microscopy is one of the fundamental techniques suitable not only for imaging samples with atomic resolution but it can also be used together with spectroscopic techniques, such as electron energy–loss spectroscopy, which is capable of detecting energy transfer between the electron beam and probed sample. One of the new possibilities is to employ vortex electron beams, which in the interaction with samples exchange energy and also orbital angular momentum that is manifested in dichroism in electron energy–loss spectra. The use of electron vortices is especially suitable for probing chiral or magnetic samples whose response would be otherwise undetectable.

In this thesis, the interaction of vortex electrons with chiral nanostructures (e.g. plasmonic antennas of special shapes) will be explored. Both numerical and analytical descriptions will be used in limiting cases. One of the possible goals will be to find experimental conditions and parameters (e. g. focusing of the beam, magnitude of the orbital angular momentum, initial beam energy) for maximization of the detected dichroic signal.

### **Bachelor's Thesis goals:**

- 1) Review of electron energy–loss spectroscopy (EELS) and vortex electron beams (VEBs). Study the possibilities of theoretical description of inelastic interaction of VEBs with different types of samples.
- 2) Model analytically EELS for VEBs interacting with point chiral objects. Try to find computationally suitable experimental parameters for the maximisation of dichroic EELS signal.
- 3) Get to know existing programmes for the numerical solution of Maxwell's equations (e.g., Comsol Multiphysics, MNPBEM toolbox for Matlab) and try to implement the interaction of VEBs with chiral nanostructures within these programmes.

**Recommended bibliography:**

GARCÍA DE ABAJO, F. J. Optical excitations in electron microscopy. *Rev. Mod. Phys.*, 82 (2010), 209-275.

ASENJO-GARCÍA A., and GARCÍA DE ABAJO, F. J. Dichroism in the interaction between vortex electron beams, plasmons, and molecules. *Phys. Rev. Lett.*, 113 (2014), 066102.

ZANFROGNINI, M., et al. Orbital angular momentum and energy loss characterization of plasmonic excitations in metallic nanostructures in TEM. *ACS Photonics*, 6 (2019), 620-627.

Deadline for submission Bachelor's Thesis is given by the Schedule of the Academic year 2021/22

In Brno,

L. S.

---

prof. RNDr. Tomáš Šikola, CSc.  
Director of the Institute

---

doc. Ing. Jaroslav Katolický, Ph.D.  
FME dean

---

# Objectives which should be achieved

1. Review of electron energy-loss spectroscopy (EELS) and vortex electron beams (VEBs).  
**Study the possibilities of theoretical description of inelastic interaction of VEBs with different types of samples.**
2. Model analytically **EELS for VEBs interacting with point chiral objects**. Try to find computationally suitable experimental parameters for the **maximisation of dichroic EELS signal**.
3. Get to know existing programmes for the numerical solution of Maxwell's equations (e.g., Comsol Multiphysics, MNPBEM toolbox for Matlab) and try to implement the interaction of VEBs with chiral nanostructures within these programmes.

## Raw Outline of the Thesis

### Introduction

1. Chirality and dichroism
  - What does chirality mean?
    - Picture of hands (etymology of the term)
    - Properties of chiral structures?
    - Chirality of molecules – examples!
    - Properties of chiral molecules
      - + Optical Activity (mechanism? and use in spectroscopy)
      - + Chirality and enantiomers – Drugs and Healthcare (Thalidomide)
    - Chirality of VEBs and their properties
  - Measurement and Dichroism
    - dichroism (literally, "two-colored")
    - dichroism in nature (bug shells etc.)
2. Electron energy loss spectroscopy (EELS) with Vortex Electron Beams (VEBs)
  - Principles of method
  - EEL spectrum function
  - Vortex electron Beams (VEBs)
    - Theory of VEB formation +Lauge-Gaussian beams
    - Methods of preparation
    - Properties of VEBs (in comparison with standard electron beams)
    - Analytical model
3. Semi-Analytical model of VEB's interaction with a chiral point object
  - Maximization of dichroic EEL spectrum
4. Numerical analysis

- 
- Boundary Element Method (BEM)
    - derivation from Maxwell's equations
  - Numerical model of VEB's interaction with a nanohelix using MNPBEM toolbox for Matlab

## Abstract

  Lorem ipsum dolor sit amet, consectetur adipisici elit, sed eiusmod tempor incididunt ut labore et dolore magna aliqua. Ut enim ad minim veniam, quis nostrud exercitation ullamco laboris nisi ut aliquid ex ea commodo consequat. Quis aute iure reprehenderit in voluptate velit esse cillum dolore eu fugiat nulla pariatur. Excepteur sint obcaecat cupiditat non proident, sunt in culpa qui officia deserunt mollit anim id est laborum. »>XXX«<

## Key Words

  EELS, Vortex electron beams, optical dichroism

## Abstrakt

  Měsíční kamení říká, že bědovat nad šedivostí dábelských démonů češství, ťukaje si na čelo, dým nepřináší a život ani úpění skřehotajících žab na slat nevrátí, člověka nevyžene a kočka bude mňoukat dál.

## Klíčová slova

  OŠMERA, Martin. *Optical dichroism in vortex electron energy-loss spectroscopy*. Brno, 2022. URL: <https://www.vutbr.cz/studenti/zav-prace/detail/139390>. Bachelor's thesis. Brno University of Technology, Faculty of Mechanical Engineering, Institute of Physical Engineering. Supervisor Andrea Konečná.



## Acknowledgement

Hereby I thank...



# Contents

<b>Introduction</b>	<b>1</b>
<b>1 Electron Energy-Loss Spectroscopy with Vortex Electron Beams</b>	<b>3</b>
1.1 Vortex Electron Beams (VEBs) . . . . .	4
1.1.1 Theoretical Description of VEB Formation . . . . .	5
1.1.2 Practical Methods of VEB preparation . . . . .	8
1.2 Inelastic Interaction of a VEB with a Point-like Polarizable Particle . . . . .	9
1.2.1 Modelled Experimental Setup . . . . .	11
1.2.2 Energy Loss Probability Spectrum . . . . .	11
1.3 About Electron Energy Loss Spectroscopy . . . . .	16
<b>2 Semi-Analytical Model of VEB's Interaction with chiral point object</b>	<b>19</b>
2.1 Green's Response Tensor . . . . .	19
2.1.1 Drude Model for Relative Permitivity . . . . .	22
2.1.2 Polarizability Tensor of a Sphere . . . . .	23
2.2 Implementation . . . . .	23
2.3 Results . . . . .	25
<b>3 Numerical Model</b>	<b>33</b>
3.1 Boundary Element Method . . . . .	34
3.2 Interaction of Electron Beam with the Specimen . . . . .	35
3.3 Implementation and Choice of Computation Parameters . . . . .	36
3.4 Results . . . . .	36
<b>Summary</b>	<b>39</b>
<b>Appendices</b>	<b>39</b>
<b>A Some More Calculated Spectra</b>	<b>41</b>
<b>B Notes on Math</b>	<b>45</b>
B.1 Square Root Approximation . . . . .	45
B.2 Cylindrical coordinates . . . . .	45
B.3 Evaluation of integral (1.16) using Jacobi–Anger expansion . . . . .	46
<b>List of Symbols</b>	<b>49</b>
<b>List of Abbreviations</b>	<b>51</b>

References	53
------------	----

# Introduction



# Chapter 1

## Electron Energy-Loss Spectroscopy with Vortex Electron Beams

Through the last century, the need of mankind to look at small things grew rapidly. One of the approaches used to gain better spatial resolution is to enslave electrons instead of photons. Electrons are particles with a non-zero rest mass. Thanks to that, we can get the same spatial resolution with much less energy in imaging with electrons compared to light. It is also incomparably easier to manipulate (focus) charged particles as electrons compared to high-energy light such as x-rays.

The first step in electron microscopy is the generation of free electrons. This is done by pulling the electrons from a cathode by electric field. The cathode can be heated to lower the difference between thermal energy of the electrons in the specimen and work function of the cathode. However, in state-of-the-art designs of electron microscope, cold (room temperature) cathode is used, mainly because the resulting electron beam has a narrower energy distribution. This is called field emission.

Electrons pulled from the cathode are then collimated and shaped into a well-controlled beam. Electron optics consisting of electrostatic and magnetic lenses is used to focus and further manipulate the beam e. g. for scanning. The beam profile can be further modified for different uses. Nowadays, beam currents can be so low that less than one electron is present in the microscope column at one moment. The beam amplitude profile can be then understood as the square modulus of the electron's wave function. As we will demonstrate in Secs. 1.1.1 and 1.1.2 electron beams can be tailored not only in amplitude but in the phase domain, too.

There are generally two types of electron microscope designs, scanning and transmission. In a Scanning Electron Microscope (SEM) the electron beam is scanned over the specimen and different types of emitted particles (e.g. secondary electrons, Auger electrons, backscattered electrons, cathodoluminescence, x-ray etc.) are detected, revealing different pieces of information about the point on specimen in which the beam is currently directed. The image is then constructed by attributing the measured signal to each point of the rastered mesh. The specimen can be thick (it has to fit into the microscope chamber) but must be conductive. Non-conductive specimens are thus covered by a thin metallic layer.

The second class of electron microscopes are Transmission Electron Microscopes (TEMs) which work similarly as traditional optical microscopes in which the light transmits through the specimen. Transmitted electrons construct an image on a screen which is captured by camera or directly on a CCD chip. Should electrons pass through the specimen, we typically need much higher accelerating voltage and very thin specimens ( $\lesssim 100$  nm, this is probably

the main disadvantage of TEM). Electrons in a typical TEM have energies around 30 keV (with speed  $0.33c$ , where  $c$  is the speed of light in vacuum) but can reach up to 300 keV ( $0.78c$ ). Such electron beams can be focused to spot with diameter  $\lesssim 0.1$  nm [1, 16], which leads to a very good lateral resolution since interatomic distances are typically in orders of  $10^{-1}$  nm.

There exists an interesting combination of both previous approaches: Scanning Transmission Electron Microscopy (STEM). In STEM, a high energy electron beam is scanned over a thin specimen. Several signals can be measured: transmitted electrons, high-angle diffracted electrons, cathodoluminescence etc. Beside the topographic view, STEM can be operated in a tomographic mode getting us full 3D spatial information about specimens.

We need not only to see the topography of the specimens but also to characterize their material excitations residing in them (in the best scenario together with the spatial layout). For this purpose STEM offers several spectroscopic methods (e.g. cathodoluminescence (CL) or energy dispersive x-ray (EDX) spectroscopy). Another widely used technique is Electron Energy-Loss Spectroscopy (EELS) which is preferentially used in Scanning Transmission Electron Microscopy (STEM). This method enables us to characterize and understand the specimen excitations via electron energy loss spectral function (spectrum) (EELSF) which will be discussed later in Sec. 1.3.

## 1.1 Vortex Electron Beams (VEBs)

Before we present electron vortices (vortex electron beams, VEBs), we should mention their predecessors in light. When circularly polarized, photons carry spin angular momentum  $\pm\hbar$  where the sign depends on the direction of spin of the polarization vector. This was shown in 1935 by Beth [4]. Linearly polarized photons can carry angular momentum in the direction of propagation, too. It is called orbital angular momentum (OAM) and is quantized by topological charge  $l$ , so that the total OAM magnitude is  $l\hbar$ . The wavefront of photon carrying OAM can be written, for instance, as

$$\psi_{\text{LG}}(r, \phi) \propto e^{i l \phi} L(r), \quad (1.1)$$

where  $L(r)$  is the Laguerre function dependent on polar coordinates  $r$  and  $\phi$ . [22]

This led physicists to think about an analogue in electron beams. It is known that electrons have spin angular momentum  $\pm\hbar/2$ . OAM is trivially carried by bound electrons in atoms or molecules. For free electrons, such as those in electron microscopes, the concept of OAM was demonstrated in 2010. First to produce VEBs were Uchida and Tonomura [19] and Verbeeck et al [22]. About the methods of preparation we further write in Sec. 1.1.2.

Electrons carrying OAM differ from photons in several aspects. They have charge, mass and always have spin momentum. They thus react to electromagnetic field and they can be used to probe circular magnetic dichroism [22]. There is also (as we will explain more deeply later) a possibility to use VEBs to study dichroism in chiral materials and nanostructures. Verbeeck [23] also showed that VEBs can be used (similarly as optical tweezers) to manipulate and rotate nanostructures in space.

In the center of the vortex, there is a phase singularity. This singularity makes the vortex beam chiral, which means that the vortex is not same as its mirror image, i.e.  $\psi_{+l} \neq \psi_{-l}$ . Phase singularities can be observed in nature as well as chirality, which has enormous importance in biology and chemistry. There exists a lot of molecules such as DNA (deoxyribonucleic acid), proteins, other polymers or simple molecules with four different groups attached

## 1.1. VORTEX ELECTRON BEAMS (VEBS)

---

to one carbon atom which are chiral. A lot of chiral molecules exist naturally only in one enantiomer, or the enantiomers have completely different behaviours. If a chiral structure  $A$  (e.g. the VEB) interacts with two enantiomorphs of a chiral structure  $B$  and  $\bar{B}$ , the symmetry is broken and we can expect different responses from  $AB$  vs.  $A\bar{B}$  interaction. This phenomenon can be called dichroism and is studied in this thesis.

Electron vortices probably appear commonly in everyday TEM measurements (e.g. in materials with varying thickness) and Uchida suggests they could be used in contrast enhancement [19].

IF TIME WILL BE, ADD ISUALISATIONS OF VORTICES.

### 1.1.1 Theoretical Description of VEB Formation

In this section, we will show a relatively simple derivation of a formula for a wave function corresponding to a VEB used later within this work. We start with the stationary Schrödinger's equation

$$\hat{\mathbf{H}}\psi = E\psi, \quad (1.2)$$

where  $E$  is a constant (with the meaning of energy) and the Hamiltonian for a free electron of mass  $m$  can be written as

$$\hat{\mathbf{H}} = -\frac{\hbar^2}{2m}\nabla^2, \quad (1.3)$$

with  $\hbar$  denoting the reduced Planck's constant. It can be shown, by simple substitution into the Schrödinger's Eq. (1.2), that a plane wave propagating along the  $z$  axis described as

$$\psi(x, y, z) = \psi(z) = \psi_0 \exp(i q_z z), \quad (1.4)$$

where  $\psi_0$  is a complex amplitude of the wave and  $q_z$  its wave vector, is a solution of the equation if and only if

$$E = \frac{\hbar^2 q_z^2}{2m}. \quad (1.5)$$

However, such wave function can not be normalized through the whole space. This should be no problem if we assume that the electron is captured in a finite volume (e.g. the electron microscope), which however has dimensions much larger than the electron wave function's wavelength. Near the center of the potential pit, such wave function will be very similar to the wave function of the free electron. Thus we can normalize the wave function only through the volume of the pit. Similar reasoning can be used in the center of a wavepacket [5].

We now examine the plane wave function impinging on a semi-permeable phase plate. We will consider this plate to be infinitesimally thin, allowing us to describe it by a simple complex function of transmission  $T(x', y')$  defined for the  $x', y'$  plane perpendicular to  $z$  axis at the coordinate  $z'$ , in which we have positioned the phase plate as schematically shown in Fig. 1.1. From the law of conservation of energy, such function must fulfil the condition  $|T(x', y')| \leq 1$ . Concrete real-world realisations of such plates will be discussed in Sec. 1.1.2.

Just after the wave passes through the plate, the wave function changes to  $\psi_t = T\psi_i$ , where  $\psi_i$  is the wave function just before the phase plate. By applying the Huygens principle, every point on the wave front is by itself a source of spherical wave. In the paraxial approximation it is sufficient to consider the wave to spread evenly in all directions. This leads us to solving the diffraction integral.

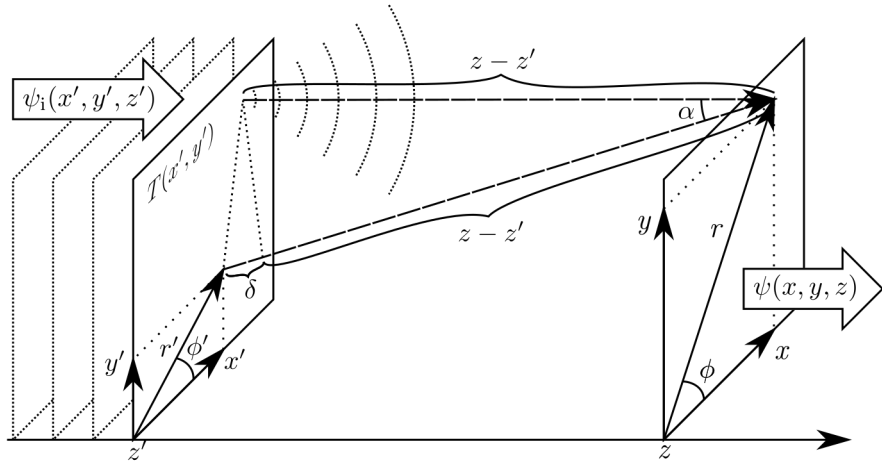


Figure 1.1: Scheme for the construction of the diffraction integral.

To find the wave propagating beyond the plane  $z'$  to a plane  $z > z'$ , we can integrate all the contributions of spherical waves coming from points of plane  $z'$ . The spherical wave with wave number  $q$  coming from a point  $\mathbf{r}'$  to a point  $\mathbf{r}$  with an initial complex amplitude  $\psi_0$  can be written as

$$\psi_{\mathbf{r}'}(\mathbf{r}) = \psi_0 \frac{e^{i q |\mathbf{r} - \mathbf{r}'|}}{|\mathbf{r} - \mathbf{r}'|}, \quad (1.6)$$

where the denominator is a consequence of the law of conservation of energy. To find the total wave, we need to integrate over all the source points. In our particular case this will be the phase plate and using notation depicted in Fig. 1.1, we can find the wave in any point of the  $z$  plane as

$$\psi(x, y, z) = -\frac{i q_z}{2\pi} \iint dx' dy' \psi_i(x', y', z') T(x', y') \frac{e^{i q_z (z - z' + \delta)}}{z - z' + \delta} \quad (1.7)$$

where we have assumed that electron is moving mainly along  $z$  axis so that  $q_x, q_y \ll q_z \approx q$ . The prefactor  $-i q_z / 2\pi$  corrects the amplitude and phase of the secondary waves, as shown in [12].

Being in the paraxial space, we may use the square root approximation rule (see B.1) and from the geometry of the problem, we can find the path deviation  $\delta$  (which is responsible for the interference at  $z$  plane) as

$$\delta = |\mathbf{r} - \mathbf{r}'| - (z - z') = (z - z')' \left[ \sqrt{1 + \frac{(x - x')^2 + (y - y')^2}{(z - z')^2}} - 1 \right] \approx \frac{(x - x')^2 + (y - y')^2}{2(z - z')}, \quad (1.8)$$

Thanks to the paraxial approximation, we can assume that for the denominator of the integrand in Eq. (1.7)  $z - z' + \delta \approx z - z'$ . With these simplifications, we can pull some terms in front of the integral and get

$$\psi(x, y, z) = -\frac{i q_z}{2\pi} \frac{e^{i q_z (z - z')}}{z - z'} \iint dx' dy' \psi_i(x', y', z') T(x', y') \exp \left[ i q_z \frac{(x - x')^2 + (y - y')^2}{2(z - z')} \right]. \quad (1.9)$$

## 1.1. VORTEX ELECTRON BEAMS (VEBS)

---

From now on, it will be convenient to work in cylindrical coordinates. Using the transformation rules (see B.2) we get the integral in Eq. (1.7) transformed as

$$\begin{aligned} \psi(r, \phi, z) = & -\frac{i q_z}{2\pi} \frac{\exp\left[i q_z \left(z - z' + \frac{r^2}{2(z - z')}\right)\right]}{z - z'} \\ & \times \iint r' dr' d\phi' \psi_i(r', \phi', z') T(r', \phi') \exp\left[\frac{i q_z}{2(z - z')}\left(r'^2 - 2rr' \cos(\phi - \phi')\right)\right]. \end{aligned} \quad (1.10)$$

If we now assume that the wave incident on phase plate is a simple plane wave  $\psi_i(r', \phi', z') = \psi'_0 \exp(i q_z z')$  in the  $z'$  plane, we can write

$$\begin{aligned} \psi(r, \phi, z) = & -\frac{i q_z}{2\pi} \frac{\psi'_0 \exp(i q_z z)}{z - z'} \exp\left(\frac{i q_z r^2}{2(z - z')}\right) \\ & \times \iint r' dr' d\phi' T(r', \phi') \exp\left[\frac{i q_z}{2(z - z')}\left(r'^2 - 2rr' \cos(\phi - \phi')\right)\right]. \end{aligned} \quad (1.11)$$

The equation above is still rather universal. All possible transmission functions can be used to get multifarious results of outcoming waves. Also, it is possible for multiple different  $T$ 's to result into similar waves. We shall now have a look at a particular example, where the transmission function takes the form

$$T(r', \phi') = e^{il\phi'} \quad \text{for } l \in \mathbb{Z}. \quad (1.12)$$

This transmission function characterizes a non-absorbing ( $|T| = 1$  in every point) phase plate with a singularity in the middle. It might be surprising that such function is practically well-achievable, as we'll show later. Finally, our resulting wave function will be

$$\begin{aligned} \psi_l(r, \phi, z) = & \frac{-i q_z \psi'_0 \exp(i q_z z)}{2\pi(z - z')} \exp\left(\frac{i q_z r^2}{2(z - z')}\right) \\ & \times \iint r' dr' d\phi' e^{il\phi'} \exp\left[\frac{i q_z}{2(z - z')}\left(r'^2 - 2rr' \cos(\phi - \phi')\right)\right]. \end{aligned} \quad (1.13)$$

Analytical solution of the integral above can be found in [2].

In practice, however, the beam from the diffraction plate is often focused by electromagnetic lenses to the specimen plane. Transmission through an ideal thin focusing lens is then described by another exponential function

$$F(r') = \exp\left(-i q_z \frac{r'^2}{2f}\right), \quad (1.14)$$

where  $f$  is the focal length of the lens. If the lens plane coincides with the phase plate, its transmission function is added in the original diffraction integral:

$$\begin{aligned} \psi_l(r, \phi, z) = & -\frac{i q_z \psi'_0 \exp(i q_z z)}{2\pi(z - z')} \exp\left(\frac{i q_z r^2}{2(z - z')}\right) \iint r' dr' d\phi' e^{il\phi'} \exp\left(-i q_z \frac{r'^2}{2f}\right) \\ & \times \exp\left(i q_z \frac{r'^2}{2(z - z')}\right) \exp\left[i q_z \frac{-rr' \cos(\phi - \phi')}{z - z'}\right]. \end{aligned} \quad (1.15)$$

If  $f = z - z'$ , the two exponentials in the first line come off leaving us with

$$\psi_l(r, \phi, z) = -\frac{i q_z \psi_0 \exp(i q_z z)}{2\pi} \exp\left(\frac{i q_z r^2}{2(z - z')}\right) \iint r' dr' d\phi' e^{i l \phi'} \exp\left[i q_z \frac{-rr' \cos(\phi - \phi')}{z - z'}\right]. \quad (1.16)$$

As shown in Appendix B.3, the integral in  $\phi'$  can be solved analytically and we obtain

$$\psi_l(r, \phi, z) = -i q_z \frac{i^l \psi_0 \exp(i q_z z)}{z - z'} \exp\left(\frac{i q_z r^2}{2(z - z')}\right) e^{i l \phi} \int_0^R r' dr' J_l\left(-q_z \frac{r r'}{z - z'}\right), \quad (1.17)$$

where  $R$  is the radius of an aperture. From similar triangles, we can find that

$$q_{r'} = \frac{q_z r'}{z - z'} \quad (1.18)$$

and the last integration can be performed in the wavenumber  $q_{r'}$  domain. We use following expression for initial VEBs assuming that they are coming from an aperture of radius corresponding to maximal perpendicular wave number  $Q_a$ :

$$\psi_l(r, \phi, z) = \frac{1}{Q_a \sqrt{\pi}} \int_0^{Q_a} dq q J_l(q r). \quad (1.19)$$

### 1.1.2 Practical Methods of VEB preparation

In this section, we will show that previous theoretical assumptions are reasonable to make since phase plates yielding transmission functions similar to those we postulated in Eq. (1.12) are practically well-achievable.

Several methods of VEB preparation have been demonstrated. The first to prepare VEB intentionally were Uchida and Tonomura in 2010 [19]. They have used graphite from a pencil in which they found structures with a thickness singularity in the middle. As the electrons impinging at the phase plate at different transverse coordinate, they penetrate the material of varying thickness. The electrons are then delayed proportionally to the thickness and a vortex can be formed. This, however, is not very practical way of vortex preparation since due to the challenging preparation of such phase plate it is not easily replicable.

To measure if they really have prepared the vortices, Uchida and Tonomura used electron holography. From it a typical "fork" pattern arises, as is shown in Fig. 1.2b. We can reverse this process and let plane wave impinge on a diffraction grating prepared in the shape of the fork (Fig. 1.2c) using focused ion beam (FIB) milling. This way, we can create vortices of opposite topological charges diverted from the main beam as is shown in Fig. 1.2d [22]. These holograms can be computer-computed and prepared for higher topological charges and used also as OAM filters by diverting the chosen vortex in a specific angle.

Spiral zone plates are similar in the production method (FIB) to the fork phase plates. They take shape shown in Fig. 1.2e. [21, 17] Today, even more sophisticated patterns are being used for measuring sorting vortex states. Such phase plate as shown in [14] could be used as the proposed OAM filter in our experiment.

Vorticity can also be imprinted into the beam by applying electromagnetic (EM) field from surface plasmon polaritons generated by elliptically polarized LASER beam illuminating a circular slit in metal. [20]

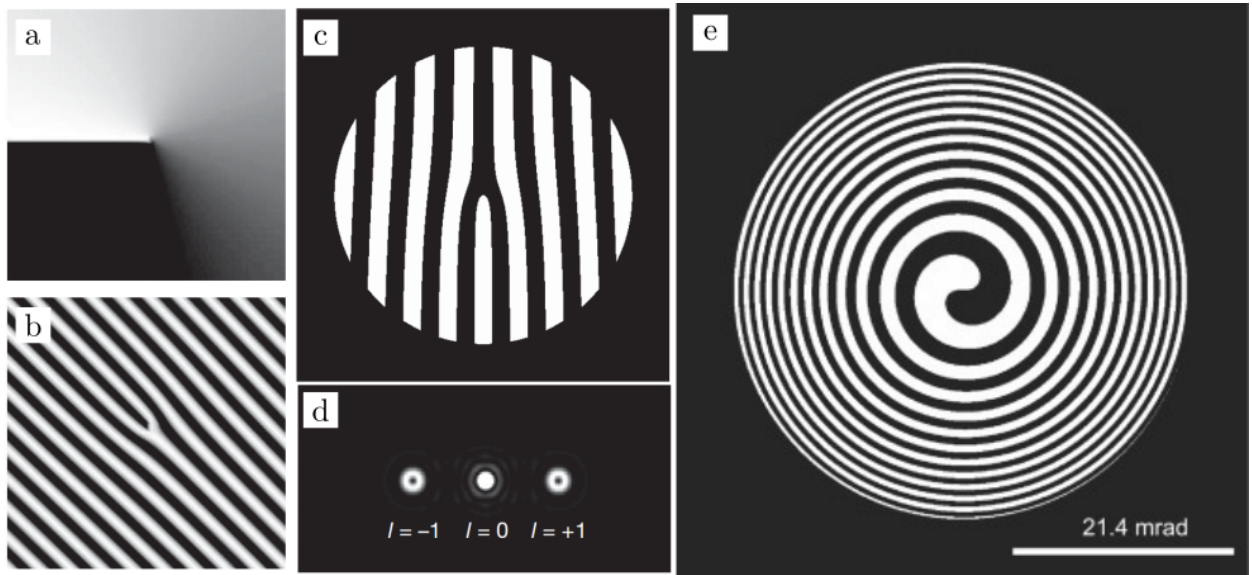


Figure 1.2: Measurement and Preparation of VEBs, Uchida [19] (a,b) and Verbeeck [22, 21] (c,d,e). a) phase profile of an ideal vortex. b) "fork" – hologram formed by interference of  $l = 1$  vortex with plane wave. c) "fork" used by Verbeeck to prepare VEBs. d) profile of the beam generated by Verbeeck with difraction fork in (c). e) spiral zone plate for VEB preparation.

One of the most promising designs of phase plates for preparation of vortex (or other phase-tailored) electrons is a programmable array of microscopic electrodes which can take form of einzel (unipotential) lenses. Einzel lens consists of three hollow electrodes in a row. The first and the last electrode have the same potential (often they are grounded). The middle electrode has different (and variable) potential. Passing through the lens, the electron effectively slows down so it is retarded in phase. Depending on the potential profile forced on the electrodes arranged in an array, phase of the electron wave is delayed differently in different parts of the beam and vortex can be formed from plane wave. [24] In Figs. 1.3 and 1.4 we have modelled several VEBs prepared by einzel-lens-PPPs of different designs.

More complicated designs of nano-electrode devices enabling the preparation of VEBs with topological charge as high as 1000 have been showed [18].

Add my figures if there is time. Maybe add figures from the articles.... In figures ... we have modelled some VEBs prepared by interaction with ideal phase plate and einzel-lens design in a "square chip" and "cylinders around circle" configurations.

## 1.2 Inelastic Interaction of a VEB with a Point-like Polarizable Particle

In this section, we will build on the wave function of the vortex electron beam (VEB) we analyzed in Sec. XXX and derive an expression for electron energy loss spectrum (or spectral function EELSF) considering well-defined initial and final vortex states.

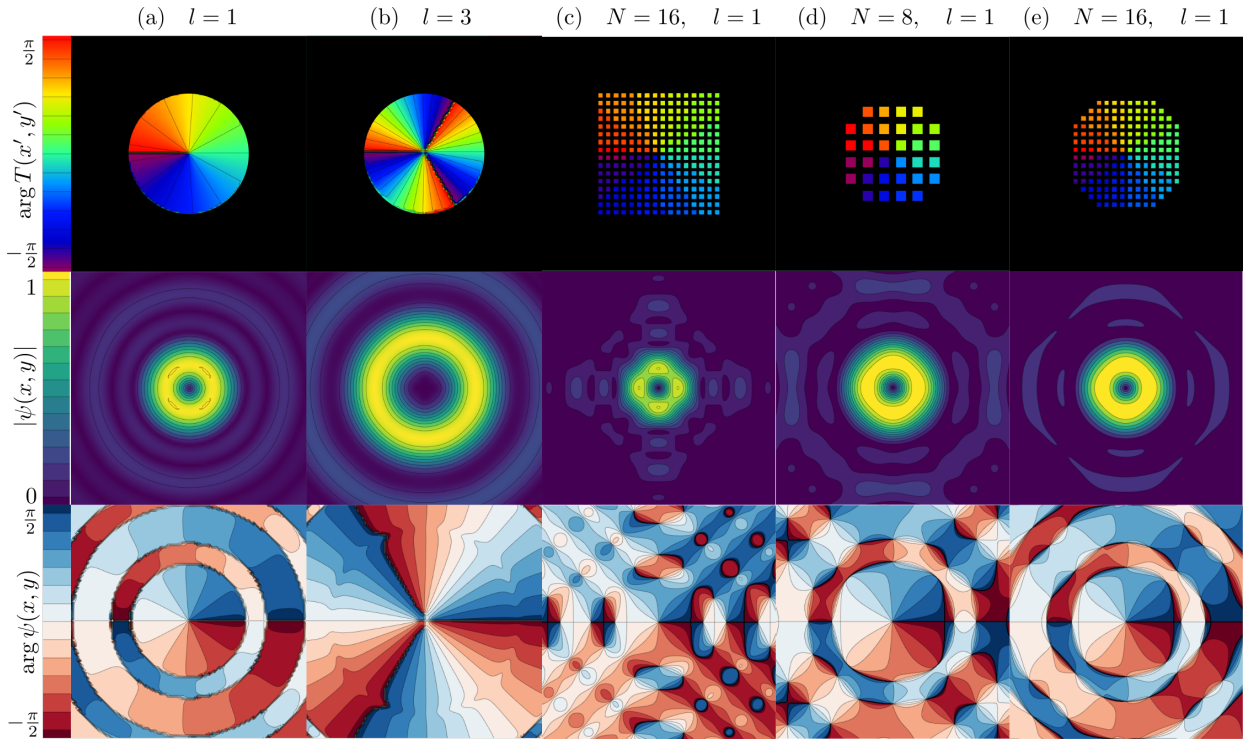


Figure 1.3: An example of VEBs prepared by ideal phase plates for two different topological charges (a, b) and using square-matrix of einzel lenses (c, d, e) retarding the wave function by factor of phase in first row. Note that the wave function produced in cases d and e is already quite near the ideal state (a).

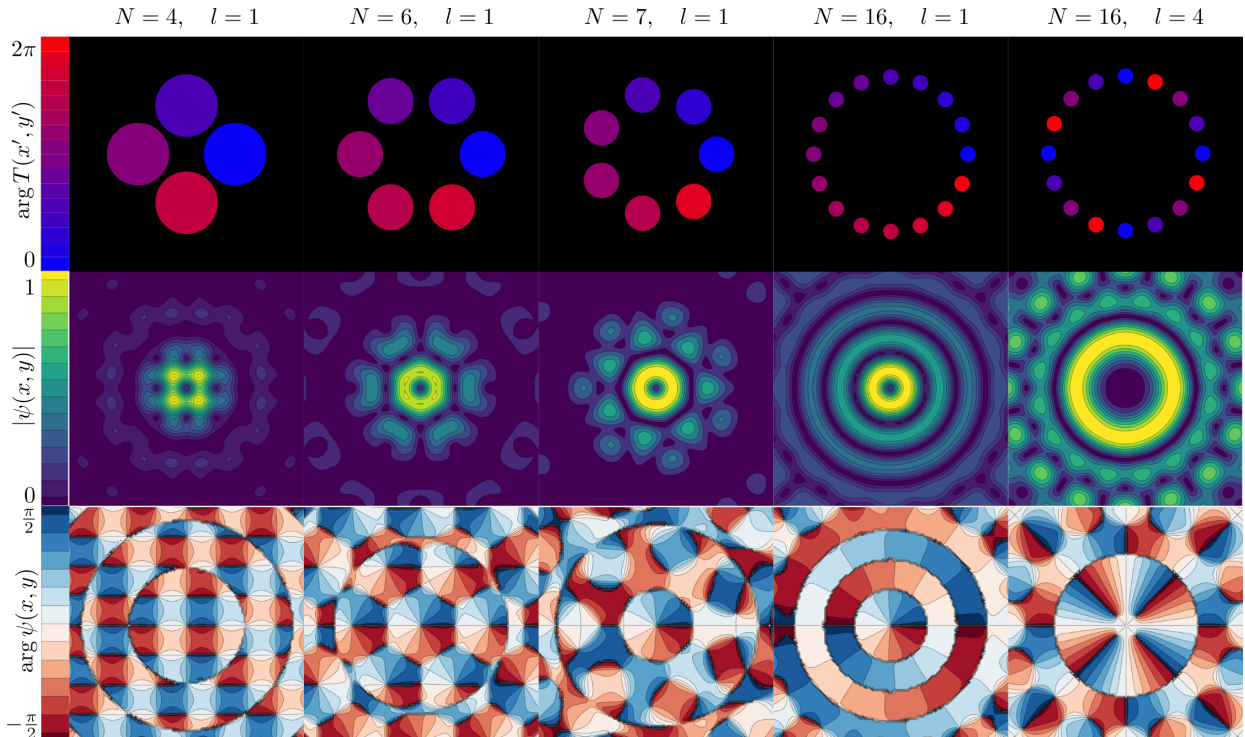


Figure 1.4: Another example of VEBs prepared by round einzel lenses arranged around circle. Note that for  $N = 4$  the square symmetry manifests significantly. For higher numbers of lenses, however, produced vortex are getting better fast.

### 1.2.1 Modelled Experimental Setup

The setup of the modelled experiment is captured in Fig. 1.5. VEBs prepared in the beam shaper interact with the specimen and can lose energy and sometimes OAM, which leads to a change of topological charge of the electron. The interaction mechanism is more precisely discussed in Sec. 2.1. After the interaction, the electron is in a superposition of all possible states. From those, one particular vortex state is chosen with an OAM sorter. EELS is then measured for a specific topological charge transition  $l_i \rightarrow l_f$ .

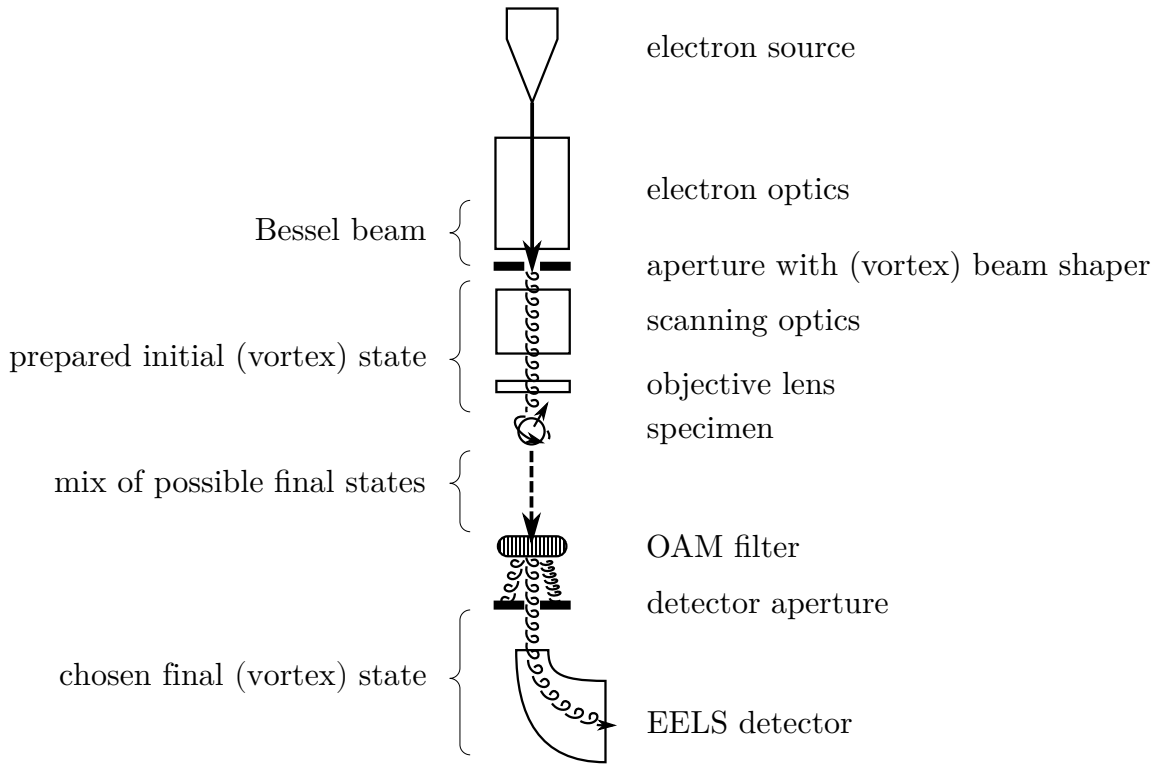


Figure 1.5: A simple schematic of modeled experiment. Electrons from a cathode are accelerated to the desired energy and monochromated (monochromator is not shown in the figure). Traveling through series of optical elements, electrons reach an aperture with a beam shaper (phase plate) and an electron vortex is formed. This electron vortex is projected onto the specimen and interacts with it. With possible use of subsequent optics (not shown), the beam hits an OAM filter which separates a chosen vortex state from the mix emerging from the interaction with specimen. Finally, the electrons are measured by EELS.

### 1.2.2 Energy Loss Probability Spectrum

Below we present a model based on the first-order perturbation theory. Subsequent paragraphs follow the references [13, 1].

We will work in cylindrical coordinates  $(r, \phi, z)$ , see App. B.2 and consider electrons moving along the  $z$  axis. The non-relativistic wave function of VEB with topological charge

$l$  can be expressed as a function  $\psi_l$  of form

$$\psi_l(r, \phi, z) = \frac{1}{\sqrt{L}} e^{i q_z z} \psi_{l,\perp}(r, \phi). \quad (1.20)$$

Here, we expressed the function as a product of two independent functions. The first being  $z$ -dependent phase factor dependent on wave vector's  $z$  component  $q_z = m_e v / \hbar$  (here expressed as the product of electron's mass  $m_e$  and velocity  $v$  divided by reduced Planck's constant  $\hbar$ ) with a normalization prefactor dependent on the normalization length  $L$ . The second function can be written as

$$\psi_{l,\perp}(r, \phi) = \frac{1}{\sqrt{A}} e^{i l \phi} J_l(q_r r), \quad (1.21)$$

where the normalization prefactor is dependent on the normalization area  $A$  and  $J_l$  is Bessel function of order  $l$  dependent on radial wavevector  $q_r$ . The Bessel function is responsible for the radial shape of the vortex. Its phase in the angular direction, i.e. its helicity, is governed by the exponential term  $\exp(i l \phi)$ .

Such wave function can not be normalized through infinite space, however, similar reasoning as we have discussed below the Eq. (1.5) can be used. Set of these functions for  $l \in \mathbb{Z}$  forms a complete basis of possible wave functions with such cylindrical symmetry.<sup>1</sup>

It can be shown that Eq. (1.20) is a solution of the Schrödinger equation for a free electron moving along  $z$  axis with the static orbital angular momentum (OAM) of magnitude  $l\hbar$ .

When an electron with the initial energy  $\hbar\epsilon_i$  (where  $\epsilon_i$  is frequency corresponding to the energy) interacts with the specimen, a virtual photon of frequency  $\omega$  transfers energy  $\hbar\omega$  from the electron to the specimen leaving the electron with the final energy  $\hbar\epsilon_f$ . The transition rate from an initial state  $\psi_i$  characterized by well-defined initial energy to the final state  $\psi_f$  can be expressed using the first order perturbation theory, as [3]

$$\frac{d\Gamma_{i \rightarrow f}}{dt} = \frac{2\hbar e^2}{\omega^2 m^2} \int d^3\mathbf{r} d^3\mathbf{r}' \psi_f(\mathbf{r}) \psi_i^*(\mathbf{r}') \nabla [\psi_i^*(\mathbf{r})] \cdot \text{Im} [\hat{\mathbf{G}}(\mathbf{r}, \mathbf{r}', \omega)] \cdot \nabla [\psi_i(\mathbf{r}')] \delta(\epsilon_f - \epsilon_i + \omega), \quad (1.22)$$

where  $\hat{\mathbf{G}}$  is the Green's electromagnetic response tensor of the specimen. We are able to use this equation only if it is possible to construct  $\hat{\mathbf{G}}$ . For a point-like dipolar particle (for which homogeneous field in its vicinity is considered) the response tensor is discussed in Sec. 2.1.

Consider now an initial state in the form  $\psi_i = \exp(i q_{z,i} z) \psi_{\perp,i}(\mathbf{r}_\perp) / \sqrt{L}$  and final state  $\psi_f = \exp(i q_{z,f} z) \psi_{\perp,f}(\mathbf{r}_\perp) / \sqrt{L}$ . By  $\mathbf{r}_\perp$  we denote the  $z$ -perpendicular component of position vector. We have also used notation in which gradient is split in derivatives of the perpendicular and longitudinal spatial coordinates  $\nabla = [\nabla_\perp; \partial_z]$ , where  $\nabla_\perp = [\partial_x; \partial_y]$ . After substitution of the

---

<sup>1</sup>As we have mentioned earlier, it is possible to use Laguerre functions. In our calculations, however, Bessel functions are sufficient enough and easy to work with.

preceding terms into (1.22), we get

$$\begin{aligned}
 \frac{d\Gamma_{i \rightarrow f}}{dt} &= \frac{2\hbar e^2}{L^2 \omega^2 m^2} \int d^3 \mathbf{r} d^3 \mathbf{r}' e^{i q_{z,f} z} \psi_{f,\perp}(\mathbf{r}_\perp) e^{-i q_{z,f} z'} \psi_{f,\perp}^*(\mathbf{r}'_\perp) \\
 &\quad \times e^{-i q_{z,i} z} [\nabla_\perp \{\psi_{i,\perp}^*(\mathbf{r}_\perp)\}; -i q_{z,i} \psi_{i,\perp}^*(\mathbf{r}_\perp)] \cdot \text{Im} [\hat{\mathbf{G}}(\mathbf{r}, \mathbf{r}', \omega)] \cdot \\
 &\quad \times e^{i q_{z,i} z'} [\nabla_\perp \{\psi_{i,\perp}(\mathbf{r}'_\perp)\}; i q_{z,i} \psi_{i,\perp}(\mathbf{r}'_\perp)] \delta(\epsilon_f - \epsilon_i + \omega) = \\
 &= \frac{2\hbar e^2}{L^2 \omega^2 m^2} \int d^3 \mathbf{r} d^3 \mathbf{r}' e^{i(z-z')(q_{z,f}-q_{z,i})} \delta(\epsilon_f - \epsilon_i + \omega) \psi_{f,\perp}(\mathbf{r}_\perp) \psi_{f,\perp}^*(\mathbf{r}'_\perp) \\
 &\quad \times [\nabla_\perp \{\psi_{i,\perp}^*(\mathbf{r}_\perp)\}; -i q_{z,i} \psi_{i,\perp}^*(\mathbf{r}_\perp)] \cdot \text{Im} [\hat{\mathbf{G}}(\mathbf{r}, \mathbf{r}', \omega)] \cdot [\nabla_\perp \{\psi_{i,\perp}(\mathbf{r}'_\perp)\}; i q_{z,i} \psi_{i,\perp}(\mathbf{r}'_\perp)]. \tag{1.23}
 \end{aligned}$$

Now we will express the loss probability for a given energy (frequency  $\omega$ ). The time  $T$  it takes one electron to move along path of length  $L$  on the  $z$  axis with speed  $v$  is  $T = L/v$ . Since our previous expression describes the (time) rate of the transition of an electron from the well-defined initial state to a specific final state, to get the overall probability of the electron transitioning to any of the final states we will need to sum over all the possible final states and multiply the rate of transition by the electron-specimen interaction time (see above). From there we get the loss probability spectrum:

$$\Gamma(\omega) = \frac{L}{v} \sum_f \frac{d\Gamma_{i \rightarrow f}}{dt}. \tag{1.24}$$

The sum over all states can be replaced by integral over all possible final-state wavevectors. Below we split the sum into summation over the perpendicular component of wavevector and another summation (rewritten as integral) over the  $z$ -component of the electron's wavevector. We further need a prefactor  $L/2\pi$  converting the wave vector  $q_{z,f}$  to its corresponding frequency  $\epsilon_f$ , resulting in

$$\Gamma(\omega) = \frac{L}{v} \sum_{f,\perp} \int dq_{z,f} \frac{L}{2\pi} \frac{d\Gamma_{i \rightarrow f}}{dt}. \tag{1.25}$$

We now combine Eqs. (1.25) with (1.23) and obtain

$$\begin{aligned}
 \Gamma(\omega) &= \frac{\hbar e^2}{v \omega^2 \pi m^2} \int d^3 \mathbf{r} d^3 \mathbf{r}' \sum_{f,\perp} \int dq_{z,f} e^{i(z-z')(q_{z,f}-q_{z,i})} \delta(\epsilon_f - \epsilon_i + \omega) \psi_{f,\perp}(\mathbf{r}_\perp) \psi_{f,\perp}^*(\mathbf{r}'_\perp) \\
 &\quad \times [\nabla_\perp \{\psi_{i,\perp}^*(\mathbf{r}_\perp)\}; -i q_{z,i} \psi_{i,\perp}^*(\mathbf{r}_\perp)] \cdot \text{Im} [\hat{\mathbf{G}}(\mathbf{r}, \mathbf{r}', \omega)] \cdot [\nabla_\perp \{\psi_{i,\perp}(\mathbf{r}'_\perp)\}; i q_{z,i} \psi_{i,\perp}(\mathbf{r}'_\perp)] \tag{1.26}
 \end{aligned}$$

Let's focus on the innermost integral of the previous expression for now:

$$\int dq_{z,f} e^{i(z-z')(q_{z,f}-q_{z,i})} \delta(\epsilon_f - \epsilon_i + \omega).$$

Energy and momentum of a particle are closely related. If we write energy expressed in terms of momentum  $p = \hbar q$  on one side of an equation and in terms of its frequency  $\epsilon$  on the other side, we get

$$\frac{(\hbar q)^2}{2m} = \hbar \epsilon, \tag{1.27}$$

thus frequency can be expressed as

$$\epsilon = \frac{\hbar q^2}{2m}. \quad (1.28)$$

We will now assume that most of the electron's energy is bound in the movement along the  $z$  axis. Thus we will be able to express all of the energy-related frequencies in terms of  $z$  components of wavevectors. In other words, we will use paraxial (or non-recoil) approximation. Because of the filtering property of the Dirac's delta  $\delta$ , the result of the integral is the integrand in which we substitute for the integrated variable the value, in which the argument of  $\delta$  is equal to zero. Using previous expression, we get

$$\begin{aligned} 0 &= \frac{\hbar q_f^2}{2m} - \frac{\hbar q_i^2}{2m} + \omega, \\ q_f &= q_i \sqrt{1 - \frac{2m}{\hbar q_i^2} \omega} \approx \\ &\approx q_i \left(1 - \frac{m}{\hbar q_i^2} \omega\right). \end{aligned} \quad (1.29)$$

The  $z$  subscripts were intentionally left out for clarity. In the last step we assumed that  $\omega \ll \epsilon_i$  and the square root approximation rule (see B.1) was used. This is a very plausible step, since the swift electron loses typically only fraction of order lower than  $10^{-3}$  of its initial energy interacting with the specimen originally in its ground state (i.e. not excited by other means) [1, p. 213].

Expanding the last term with momentum  $\hbar q_i = p = mv$ , we get

$$q_f = q_i \left(1 - \frac{\omega}{v q_i}\right). \quad (1.30)$$

Further, we substitute [from Eq. (1.28)] for  $dz_{z,f} = d\epsilon_f m / \hbar q_{z,f} = d\epsilon_f / v$ . Altogether we get

$$\int dz_{z,f} e^{i(z-z')(q_{z,f}-q_{z,i})} \delta(\epsilon_f - \epsilon_i + \omega) = \frac{1}{v} \exp\left(-i\omega \frac{z-z'}{v}\right). \quad (1.31)$$

By substituting this integral into Eq. (1.26) we get

$$\begin{aligned} \Gamma(\omega) &= \frac{\hbar e^2}{v^2 \omega^2 \pi m^2} \int d^3 \mathbf{r} d^3 \mathbf{r}' \exp\left(-i\omega \frac{z-z'}{v}\right) \sum_{f,\perp} \psi_{f,\perp}(\mathbf{r}_\perp) \psi_{f,\perp}^*(\mathbf{r}'_\perp) \\ &\times \left[ \nabla_\perp \left\{ \psi_{i,\perp}^*(\mathbf{r}_\perp) \right\} ; -i q_{z,i} \psi_{i,\perp}^*(\mathbf{r}_\perp) \right] \cdot \text{Im} \left[ \hat{\mathbf{G}}(\mathbf{r}, \mathbf{r}', \omega) \right] \cdot \left[ \nabla_\perp \left\{ \psi_{i,\perp}(\mathbf{r}'_\perp) \right\} ; i q_{z,i} \psi_{i,\perp}(\mathbf{r}'_\perp) \right] \end{aligned} \quad (1.32)$$

For further simplification, we define

$$\hat{\mathcal{G}}(\mathbf{r}_\perp, \mathbf{r}'_\perp, \omega) = \int dz dz' \exp\left(-i\omega \frac{z-z'}{v}\right) \text{Im} \left[ \hat{\mathbf{G}}(\mathbf{r}, \mathbf{r}', \omega) \right] \quad (1.33)$$

and substitute this into the Eq. (1.32); we get

$$\begin{aligned} \Gamma(\omega) &= \frac{\hbar e^2}{v^2 \omega^2 \pi m^2} \int d^2 \mathbf{r}_\perp d^2 \mathbf{r}'_\perp \sum_{f,\perp} \psi_{f,\perp}(\mathbf{r}_\perp) \psi_{f,\perp}^*(\mathbf{r}'_\perp) \\ &\times \left[ \nabla_\perp \left\{ \psi_{i,\perp}^*(\mathbf{r}_\perp) \right\} ; -i q_{z,i} \psi_{i,\perp}^*(\mathbf{r}_\perp) \right] \cdot \hat{\mathcal{G}}(\mathbf{r}_\perp, \mathbf{r}'_\perp, \omega) \cdot \left[ \nabla_\perp \left\{ \psi_{i,\perp}(\mathbf{r}'_\perp) \right\} ; i q_{z,i} \psi_{i,\perp}(\mathbf{r}'_\perp) \right]. \end{aligned} \quad (1.34)$$

For the sum in the last expression, we can again move from discrete to continuous domain. Now, it is time to decide, whether it will be best to work in Cartesian or in polar coordinates. This depends on the form of wave and the type of detector i.e. their symmetries. If the detector were square or the wave were of any arbitrary (radially non-symmetric) shape, we shall use Cartesian coordinates and integrate over the detector's  $q$ -space.

$$\sum_{f,\perp} \rightarrow \frac{A}{(2\pi)^2} \int dq_{f,x} \int dq_{f,y}. \quad (1.35)$$

As the basis for the space of wave functions  $\psi_{\perp}$ , we can then use a set of functions of the form

$$\psi_{\perp}^{(q_x, q_y)} = \frac{1}{\sqrt{A}} \exp [i(q_x x + q_y y)], \quad (1.36)$$

where  $A$  is a normalization constant.

The spectral loss function then becomes

$$\begin{aligned} \Gamma(\omega) = & \frac{\hbar e^2}{v^2 \omega^2 \pi m^2} \int dx dy dx' dy' \frac{A}{(2\pi)^2} \int dq_{f,x} e^{i q_{f,x} (x - x')} \int dq_{f,y} e^{i q_{f,y} (y - y')} \\ & [\nabla_{\perp} \{ \psi_{i,\perp}^*(x, y) \}; -i q_{z,i} \psi_{i,\perp}^*(x, y)] \cdot \hat{\mathcal{G}}(x, y, x', y', \omega) \cdot [\nabla_{\perp} \{ \psi_{i,\perp}(x', y') \}; i q_{z,i} \psi_{i,\perp}(x', y')]. \end{aligned} \quad (1.37)$$

If there exists radial symmetry in the problem, however, it might be better to use polar coordinates. In our case (when studying VEBs) it is convenient to use a basis of functions of form (1.20). These hold the vorticity of the beam naturally and can be expressed as

$$\psi_{f,\perp}(r, \phi) = \frac{1}{\sqrt{A}} e^{i l_f \phi} J_l(q_{f,r} r), \quad (1.38)$$

To move from discrete to continuous domain, we can write

$$\sum_{f,\perp} \rightarrow \frac{A}{(2\pi)^2} \int_0^{Q_c} q_{f,r} dq_{f,r} \int_0^{2\pi} dq_{f,\phi} \sum_{l_f} = \frac{A}{2\pi} \int_0^{Q_c} q_{f,r} dq_{f,r} \sum_{l_f}, \quad (1.39)$$

where we can evaluate the second integral since used basis functions are  $q_{f,\phi}$ -independent.

When the OAM sorter is used, only one basis function corresponding to the concrete chosen  $l_f$  is then needed to describe the final state, and we can leave out the sum over all possible  $l_f$ s. Loss probability spectrum for the chosen  $l_f$  is then

$$\begin{aligned} \Gamma_{l_f}(\omega) = & \frac{\hbar e^2}{2\pi^2 v^2 \omega^2 m^2} \int d^2 \mathbf{r}_{\perp} d^2 \mathbf{r}'_{\perp} e^{i l_f (\phi - \phi')} \int_0^{Q_c} q_{f,r} dq_{f,r} J_l(q_{f,r} r) J_l(q_{f,r} r') \\ & \times [\nabla_{\perp} \{ \psi_{i,\perp}^*(\mathbf{r}_{\perp}) \}; -i q_{z,i} \psi_{i,\perp}^*(\mathbf{r}_{\perp})] \cdot \hat{\mathcal{G}}(\mathbf{r}_{\perp}, \mathbf{r}'_{\perp}, \omega) \cdot [\nabla_{\perp} \{ \psi_{i,\perp}(\mathbf{r}'_{\perp}) \}; i q_{z,i} \psi_{i,\perp}(\mathbf{r}'_{\perp})]. \end{aligned} \quad (1.40)$$

This is the final expression for the energy loss spectral function (EELSF).<sup>2</sup> It describes the probability density (upon range of photon frequencies  $\omega$ ) of electron losing energy  $\hbar\omega$  if we know, that after interaction with the specimen the electron had left with final topological charge  $l_f$ . If more states with different topological charges from the set  $\{l_f\}$  are needed, the spectral loss function for those states would be a simple sum

$$\Gamma_{\{l_f\}}(\omega) = \sum_{l \in \{l_f\}} \Gamma_l(\omega). \quad (1.41)$$

<sup>2</sup>However, we do not use this exact expression to calculate our semianalytical spectra. See Sec. 2.1, precisely Eq. (2.18) for further explanation.

## 1.3 About Electron Energy Loss Spectroscopy

In the previous section we derived an expression for the Electron Energy Loss Spectral Function (EELSF) of a swift electron impinging on a polarizable point-like particle. Now we briefly examine Electron Energy Loss Spectroscopy (EELS) as an experimental technique and focus on low-energy part of the spectrum where optical excitations reside.

A moving relativistic electron acts as a broadband source of an evanescent electromagnetic field,[16] which can excite optical excitations in the specimen. In a form of photons with frequency of the field, the specimen can then gain energy. The basic principle of EELS is the Law of conservation of energy. Instead of measuring energy gained by the specimen, we measure the energy lost by electron. If we measure that the electron interacting with a specimen lost some defined energy  $\hbar\omega$ , we immediately know that the specimen must have gained the same amount of energy  $\hbar\omega$  from the interaction. The result of an EELS measurement is electron energy loss spectrum (spectral function, EELSF) denoted  $\Gamma$ . This spectrum shows the probability density of a defined energy loss and if we integrate over a specific interval of energies (frequencies) we get the probability of electron losing (thus specimen gaining) the energy (frequency) from the chosen interval.

EELS is typically measured in STEMs. By scanning over the specimen, EELS maps the specimen by interaction in the near field. The spatial resolution is thus mainly limited by the span of the evanescent field produced by the electron. Thanks to the near-field character of the interaction, we are not bound to radiative optical modes of the specimens. The fact that EELS maps all excitations is a big advantage in comparison to CL which accounts only for radiative modes, thus generally  $\Gamma_{\text{EELS}} \geq \Gamma_{\text{CL}}$ . García de Abajo and Kociak showed in [9] that in the case of geometries where translational invariance in the direction of the beam exists the EELS spectrum is proportional to the local density of optical states (LDOS) enabling us to map optical excitations directly. For more general geometries this may not hold, however in many cases it (at least qualitatively) does.

Thanks to this fact, EELS can be used to probe plasmons [6]. Nowadays even plasmon tomography is possible [16]. EELS can be angle-resolved which enables us to study structures with translational symmetries in inverse space rather than in real. The energy resolution in some setups has already lowered under 10 meV and we are able to analyze energies  $> 30$  meV, which enables us to study even phononic and vibrational excitations.

To model an interaction with optical excitations in a realistic sample, one usually has to numerically solve Maxwell's equations. Several methods are known. One of them is Boundary Element Method (BEM), which is further discussed in Ch. 3. In some cases, as is ours for the point-like particle in Ch. 2, we can bypass the numerical solution.

When the specimen is excited before (or together) with the interaction with the specimen, e.g. thermally or by an external optical stimulation, it can also give the energy to (not take it from) the electron. When this phenomenon is measured in spectra, we talk about Electron Energy Gain Spectroscopy (EEGS)

Temporal information about the interaction with the specimen can be gained from Fourier analysis of the measured data or by employing ultrafast TEM setups.

Do i need to talk about the zero loss peak????

### Structured beams in EELS

As we discussed in the Sec. 1.1 the wave functions of electrons can be tailored in multifarious ways [for example with programmable phase plates (PPPs)]. The control over the beam

### 1.3. ABOUT ELECTRON ENERGY LOSS SPECTROSCOPY

---

shape introduces new degrees of freedom which can be used to study more phenomena in a more simple and faster measurement or even open new fields of study for example in the study of magnetic structures or chiral substances of materials which are very common in nature. Beams structured in spatial or temporal domains can be viewed as "quantum probes" which can reveal all kinds of new information about specimen, since after the interaction the electron's state is entangled with the specimen's. This enables us to analyze the state of electrons by loss and gain information about the state of specimens. This can open new fields in microscopy. Last but not least, the use of structured electron beams can reduce the need for conventional electron optics (e.g., correctors) and reduce the complexity of electron microscopes columns. Thus TEMs could become smaller.



# Chapter 2

## Semi-Analytical Model of VEB's Interaction with chiral point object

### 2.1 Green's Response Tensor

In this section we will discuss the Green's response tensor needed for evaluation of EEL spectral function derived in Sec. 1.2.

For the next couple of paragraphs we roughly follow [15]. Helmholtz equation for electromagnetic field in the domain of frequencies  $\omega$  with corresponding wavenumber  $k = \omega/c$  (where  $c$  is the speed of light) in vacuum with the Lorenz gauge can be written in the following form for 4-potential  $A^i$  (thus for classical vector and scalar potentials) and 4-current  $J^i$  as

$$[\nabla^2 + k^2] A^i = -\mu_0 J^i. \quad (2.1)$$

Focus now on any one component. Assuming the charge density (or one particular component of current density) to be concentrated in one concrete (source) point  $\mathbf{r}'$  so that the total charge (current) is unit, we can rewrite the previous expression for any (field) point  $\mathbf{r}$  in space using Dirac's delta as

$$[\nabla^2 + k^2] G_0(\mathbf{r}, \mathbf{r}') = -\delta(\mathbf{r} - \mathbf{r}'), \quad (2.2)$$

where  $G_0(\mathbf{r}, \mathbf{r}')$  is some function. Since the Helmholtz operator is linear, there exists (in general) an inverse operator (traditionally called Green's operator) which acts as a response operator on the unit impulse. If this operator is known, we can then find the response for any possible impulse. In our case we can find the potential field  $A^i(\mathbf{r})$  in any point in space for any possible current density field  $J^i(\mathbf{r})$  as

$$A^i(\mathbf{r}) = \underbrace{\int d^3 \mathbf{r}' \mu_0 G_0(\mathbf{r}, \mathbf{r}') J^i(\mathbf{r}')}, \quad (2.3)$$

where we have underbraced the mentioned linear operator.

A solution for the 3D Helmholtz equation (2.2) can be found in the form

$$G_0(\mathbf{r}, \mathbf{r}') = \frac{\exp(i k |\mathbf{r} - \mathbf{r}'|)}{4\pi |\mathbf{r} - \mathbf{r}'|}. \quad (2.4)$$

The function  $G_0(\mathbf{r}, \mathbf{r}')$  is known as scalar vacuum Green's function. We can see that the expression is dependent only on the difference between  $\mathbf{r}$  and  $\mathbf{r}'$ , thus it is possible to write  $G_0(\mathbf{r}, \mathbf{r}') = G_0(\mathbf{r} - \mathbf{r}')$ .

Similarly, the Green operator can be found for electric  $\mathbf{E}$  and magnetic  $\mathbf{H}$  fields. Since those are 3-component vector quantities the Green's operator must be a tensor of rank 3.

$$\mathbf{E}(\mathbf{r}) = \frac{i}{\omega} \int d^3 \mathbf{r}' \hat{\mathbf{G}}_{EE}(\mathbf{r}, \mathbf{r}') \cdot \mathbf{J}(\mathbf{r}'), \quad (2.5)$$

$$\text{???} \quad \mathbf{H}(\mathbf{r}) = \int d^3 \mathbf{r}' \hat{\mathbf{G}}_{ME}(\mathbf{r}, \mathbf{r}') \cdot \mathbf{J}(\mathbf{r}'). \quad (2.6)$$

The current density  $\mathbf{J}$  can be further calculated from dipole moment  $\mathbf{p}$  as

$$\mathbf{J}(\mathbf{r}') = -i\omega \mathbf{p} \delta(\mathbf{r}' - \mathbf{r}_0), \quad (2.7)$$

where  $\mathbf{r}_0$  is the position of the dipole.

The Green's dyadic electro-electric function  $\hat{\mathbf{G}}_{EE}$  can be calculated from the scalar vacuum Green's function  $G_0$  as

$$\hat{\mathbf{G}}_{EE}(\mathbf{r}, \mathbf{r}') = \frac{1}{\varepsilon_0} \left[ k^2 \hat{\mathbf{1}} + \nabla' \otimes \nabla' \right] G_0(\mathbf{r}, \mathbf{r}'), \quad (2.8)$$

where  $\hat{\mathbf{1}}$  is unit operator,  $\nabla'$  is the nabla operator in respect to primed (source) position vector  $\mathbf{r}'$  and  $\otimes$  stands for tensor product. The Green's dyadic electro-magnetic function  $\hat{\mathbf{G}}_{ME}$  is then

$$\hat{\mathbf{G}}_{ME}(\mathbf{r}, \mathbf{r}') = \frac{1}{i\omega} \nabla' \times \hat{\mathbf{G}}_{EE}(\mathbf{r}, \mathbf{r}'). \quad (2.9)$$

It describes the magnetic field induced by electrical current (dipole).

From the symmetry of Maxwell's equations [13] it can be shown that Green's magneto-magnetic tensor fulfills

$$\hat{\mathbf{G}}_{MM} = \hat{\mathbf{G}}_{EE} \quad (2.10)$$

and Green's magneto-electric tensor can be found as

$$\hat{\mathbf{G}}_{EM} = -\hat{\mathbf{G}}_{ME}. \quad (2.11)$$

In Eq. (1.33) we defined (following Ref. [13]) a Green's response tensor integrated along  $z$  axes. To fully construct it, we will define

$$\begin{aligned} \hat{\mathbf{G}}_{EE}^{\text{int}}(\mathbf{r}, \mathbf{r}') &= \int dz dz' \exp\left(-i\omega \frac{z - z'}{v}\right) \hat{\mathbf{G}}_{EE} = \\ &= \frac{1}{2\pi\varepsilon_0} (k^2 \hat{\mathbf{1}} + \nabla' \otimes \nabla') \left[ e^{i\omega \frac{z_p}{v}} K_0 \left( \frac{\omega |\mathbf{r}_\perp - \mathbf{r}'_\perp|^2}{v \gamma_L} \right) \right], \end{aligned} \quad (2.12)$$

where  $K_0$  is modified Bessel's function of order 0,  $\gamma_L = 1/\sqrt{1 - v^2/c^2}$  is Lorentz factor.

Thanks to the linearity of differential operators used in derivation of dyadic functions from vacuum Green function, the previously stated relations between different Green's tensors are retained for their integrated forms:

$$\hat{\mathbf{G}}_{EM}^{\text{int}}(\mathbf{r}, \mathbf{r}') = -\frac{1}{ikc} \nabla' \times \hat{\mathbf{G}}_{EE}^{\text{int}}(\mathbf{r}, \mathbf{r}'), \quad (2.13)$$

$$\hat{\mathbf{G}}_{MM}^{\text{int}} = \hat{\mathbf{G}}_{EE}^{\text{int}}, \quad (2.14)$$

## 2.1. GREEN'S RESPONSE TENSOR

---

and

$$\hat{\mathbf{G}}_{\text{ME}}^{\text{int}} = -\hat{\mathbf{G}}_{\text{EM}}^{\text{int}}. \quad (2.15)$$

The electron moving in the microscope column generates electric and magnetic field around the specimen. This is described by the Green's electro-electric and electro-magnetic tensors. Assuming the specimen is small enough so the field around it is homogeneous we can describe it by simple polarizability tensors:

$$\begin{array}{lll} \text{electro-electric} & \mathbf{E} \rightarrow \mathbf{p} & \hat{\alpha}_{\text{EE}}, \\ \text{electro-magnetic} & \mathbf{E} \rightarrow \mu & \hat{\alpha}_{\text{ME}}, \\ \text{magneto-electric} & \mathbf{H} \rightarrow \mathbf{p} & \hat{\alpha}_{\text{EM}}, \\ \text{electro-magnetic} & \mathbf{H} \rightarrow \mu & \hat{\alpha}_{\text{MM}}. \end{array}$$

Again, thanks to the symmetry between electric and magnetic fields, in reciprocal materials we can write

$$\hat{\alpha}_{\text{ME}} = -\hat{\alpha}_{\text{EM}}^T \quad (2.16)$$

The induced electric (magnetic) dipole creates its own electric and magnetic field, which is captured, again, employing by Green's electro-electric and electro-magnetic (magneto-electric and magneto-magnetic) tensors.

It is essential to mention that if the specimen were polarizable in the crossed electric-magnetic terms  $\hat{\alpha}_{\text{EM}}$  and  $\hat{\alpha}_{\text{ME}}$ , it must always be polarizable in the electric  $\hat{\alpha}_{\text{EE}}$  and magnetic  $\hat{\alpha}_{\text{MM}}$  terms. [3]

The induced magnetic field does not change the energy of the electron. We can also assume that the trajectory of the electron is almost unchanged by the magnetic field produced by the specimen. This means that we can neglect magnetic forces acting on the electron in our computations relating EELS. To capture the whole interaction of the electron with the specimen, we then define Green's response tensor

$$\check{\mathcal{G}}(\mathbf{r}, \mathbf{r}', \omega) = \check{\mathcal{G}}_{\text{EE}}(\mathbf{r}, \mathbf{r}', \omega) = \hat{\mathbf{G}}_{\text{Ei}}^{\text{int}}(\mathbf{r}, \mathbf{r}_p, \omega) \cdot \hat{\alpha}_{ij}(\omega) \cdot \hat{\mathbf{G}}_{j\text{E}}^{\text{int}}(\mathbf{r}_p, \mathbf{r}', \omega), \quad (2.17)$$

where we have used Einstein summation rule (ESR) through indices  $i, j \in \{\text{E, M}\}$  and  $\mathbf{r}_p$  is the position of the studied particle (specimen). This tensor is in fact only electro-electric, as we have captured by the lower indices EE. However, since we don't need the magnetic ones we will omit the lower indices straight away. This is not yet the Green's response tensor defined in Eq. (2.17). However we were able to find the green response operator "without the imaginary part function" (compare Eqs. (1.33) and (2.12)). In the Eq. (1.40) the imaginary part is still inside the integrand. Fortunately, it can be pulled out [1] in front of the integral and EELSF can be calculated as

$$\begin{aligned} \Gamma_{l_i \rightarrow l_f}(\omega) = & \frac{\hbar e^2}{2\pi^2 v^2 \omega^2 m^2} \text{Im} \left\{ \int d^2 \mathbf{r}_\perp d^2 \mathbf{r}'_\perp e^{i l_f (\phi - \phi')} \int_0^{Q_c} q_{f,r} dq_{f,r} J_l(q_{f,r} r) J_l(q_{f,r} r') \right. \\ & \times \left. \left[ \nabla_\perp \left\{ \psi_{i,\perp}^*(\mathbf{r}_\perp) \right\}; -i q_{z,i} \psi_{i,\perp}^*(\mathbf{r}_\perp) \right] \cdot \check{\mathcal{G}}(\mathbf{r}_\perp, \mathbf{r}'_\perp, \omega) \cdot \left[ \nabla_\perp \left\{ \psi_{i,\perp}(\mathbf{r}'_\perp) \right\}; i q_{z,i} \psi_{i,\perp}(\mathbf{r}'_\perp) \right] \right\}. \end{aligned} \quad (2.18)$$

To grasp the interaction intuitively, a diagram of the interaction is shown in Fig. 2.1. Let's focus on this Figure now and explain intuitively what is happening. As we have already mentioned, a swift electron is a source of optical excitation thanks to its evanescent field. When a point-like particle is placed in the vicinity of the beam, it feels the field. We have

described the particle by four polarizability tensors. Two of them are "pure",  $\hat{\alpha}_{EE}$  and  $\hat{\alpha}_{MM}$ , and two of them are "crossed". In our setup we have another degree of freedom – distance between the specimen and the center of the vortex.

The pure terms account for achiral (or non-chiral) modes excited on the particle. The crossed terms are at play if the particle is chiral in nature (by material or structure). On such particle, chiral modes can be excited.

Any modes excited create their own field which acts back on the electron. This is how the electron loses its energy. After the interaction, the electron is in a superposition of all possible final states.

If not only the specimen is chiral but the electron impinging on it too, the symmetry breaks and dichroism emerges. In this context, dichroism is the effect of different response to qualitatively opposite impulses, the difference between response on right-hand vs left-hand vortex or, with the same initial topological charge  $l$ , the difference between positive  $+\Delta l$  vs negative  $-\Delta l$  change of topological charge in the interaction.

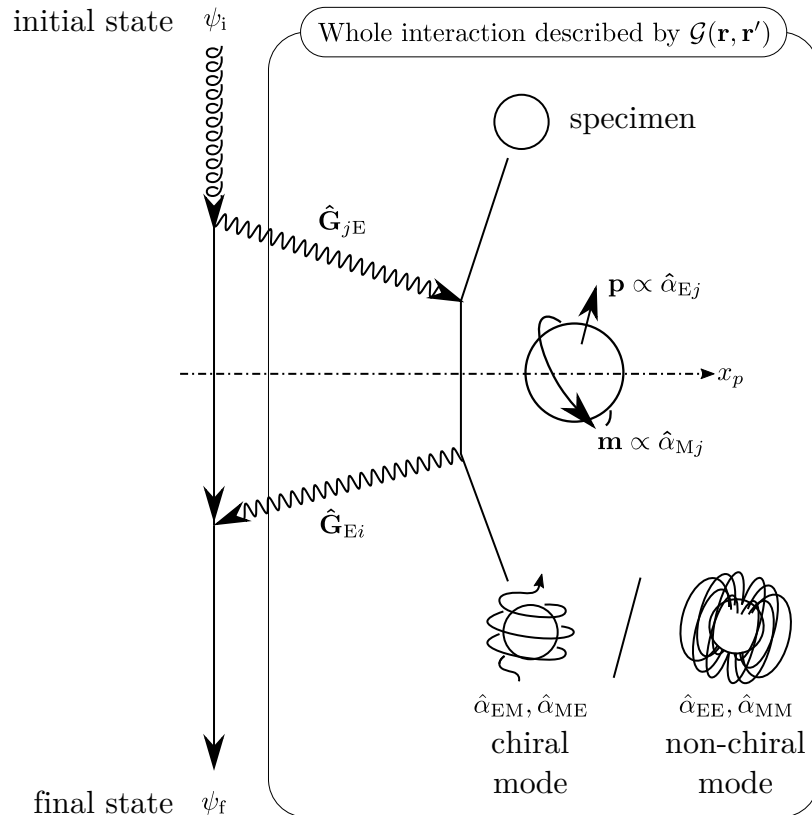


Figure 2.1: Diagram of the interaction of an electron with the specimen.

### 2.1.1 Drude Model for Relative Permittivity

Frequency-dependent relative permittivities (dielectric functions) are usually tabulated. Some metals are well characterized by the Drude free electron model which yields the relative permittivity

$$\varepsilon(\omega) = 1 - \frac{\omega_p^2}{\omega^2 + i\gamma\omega}, \quad (2.19)$$

where  $\omega_p$  is the bulk plasmon frequency of studied metal and  $\gamma$  is a small phenomenological relaxation rate which accounts for the dampening of plasma oscillation in the metal. In our calculation we used the values  $\hbar\omega_p = 9.1$  eV and  $\hbar\gamma = 0.15$  eV. [1].

### 2.1.2 Polarizability Tensor of a Sphere

Thanks to the total symmetry of a sphere, polarizability of a spherical metallic particle with radius  $a$  and relative permittivity  $\varepsilon(\omega)$  can be described by scalar function  $\alpha(\omega)$  as [3]

$$\alpha(\omega) = 4\pi\varepsilon_0 \frac{3c^3}{2\omega^3} \frac{-j_1(\rho_0) [\rho_1 j_1(\rho_1)]' + \varepsilon(\omega) j_1(\rho_1) [\rho_0 j_1(\rho_0)]'}{h_1^{(+)}(\rho_0) [\rho_1 j_1(\rho_1)]' - \varepsilon(\omega) j_1(\rho_1) [\rho_0 h_1^{(+)}(\rho_0)]'}, \quad (2.20)$$

where  $j_1(x) = \sin(x)/x^2 - \cos(x)/x$  and  $h_1^{(+)}(x) = (1/x^2 - i/x) \exp(ix)$  are spherical Bessel and Hankel functions, respectively, prime stands for differentiation with respect to the argument and  $\rho_0 = \omega a/c$  and  $\rho_1 = \sqrt{\varepsilon(\omega)} \rho_0$ . Said expression was used to gain realistic polarizability in our calculations, where we used universally the value for radius  $a = 5$  nm. Throughout our calculations we assumed diagonal polarizability tensors with equal values in each axis so that  $\hat{\alpha}(\omega) = \alpha(\omega) \cdot \hat{\mathbf{1}}$ . More complicated (non-diagonal) tensor would work too.

## 2.2 Implementation

This section will describe the implementation of calculations. After the derivation of expression for EELSF in Sec. 1.2 and derivation of Green's response tensor in Sec. 2.1 we could implement those into a computer program to calculate the spectra. We have chosen programming language PYTHON for the implementation since it is open-source and there exists a great number of libraries to use. It is well human-readable language and it is fast and easy to write. The calculation speed is not the best but it was sufficient for our purpose. The support for scientific calculations in libraries is also very good. Libraries we have used are: NUMPY, SCIPY, SYMPY, MATPLOLIB and PLOTLY.

Now we shall explain how the calculation was implemented. We can rewrite the last expression for the EEL spectral function gamma (2.18) in the following form

$$\Gamma_{lf}(\omega) = \mathcal{J}(v, \omega) \int d^2\mathbf{r}_\perp d^2\mathbf{r}'_\perp \mathcal{Q}(\mathbf{r}, \mathbf{r}') \mathcal{K}(\mathbf{r}_\perp, \mathbf{r}'_\perp, \omega, v, \psi_i), \quad (2.21)$$

where

$$\mathcal{J} = \frac{\hbar e^2}{2\pi^2 v \omega^2 m^2} \quad (2.22)$$

is the prefactor, or "Jack function";

$$\mathcal{Q} = e^{i l_f(\phi - \phi')} \int_0^{Q_c} q_{f,r} dq_{f,r} J_l(q_{f,r} r) J_l(q_{f,r} r') \quad (2.23)$$

called "the Queen function", holds the radial profile of final vortex states and the interaction change of topological charge; and

$$\mathcal{K} = \left[ \nabla_\perp \left\{ \psi_{i,\perp}^*(\mathbf{r}_\perp) \right\}; -i q_{z,i} \psi_{i,\perp}^*(\mathbf{r}_\perp) \right] \cdot \check{\mathcal{G}}(\mathbf{r}_\perp, \mathbf{r}'_\perp, \omega) \cdot \left[ \nabla_\perp \left\{ \psi_{i,\perp}(\mathbf{r}'_\perp) \right\}; i q_{z,i} \psi_{i,\perp}(\mathbf{r}'_\perp) \right] \quad (2.24)$$

called "the King function" holds the initial wave functions of vortex and can be thought of as the main interaction part of the EELSF. For great part of the calculation the King and the Queen were treated separately and the Jack (as it is only a prefactor) was introduced in the end.

Both King and Queen were held in the memory of the computer as NUMPY arrays of numbers. The calculation (numerical integration of calculated integrand 4D field) had to be performed for each point in the frequency  $\omega$  domain. Fortunately, the queen is not  $\omega$ -dependent so in order to save computational time we have preevaluated the Queen for the calculation of whole spectrum with set parameters (such are topological charge, electron energy or speed) and only the King was recalculated for each  $\omega$ -point.<sup>1</sup>

To set up the computation parameters such are the number of points in space needed or its span we have rendered several plots of Psis, Kings and Queens before running the scripts. **Plots are shown in the Fig. [XXX].** We have also ran a convergence test for the number of space points. To get a reasonable compromise between calculation accuracy and computation speed we setteled on 20 nm–30 nm wide field with 50 space points in each of four dimensions ( $x, y, x', y'$ ). That is 6 250 000 points in total. These computation parameters are well compatible with set parameters of the electron beam with energy 60 keV corresponding to speed  $0.446 c$ . We have assumed the beam to have lateral spread of 20 mrad.

Occasionally, when the mesh of our space coincides in some point with the position of specimen, NaN (Not a Number) values appear in our fields. Singularities are at these points and the values around them tend to diverge to  $\pm\infty$  and python handles them as NaNs. This is a problem in numerical integration so we had to use function `numpy.nansum()` which ignores NaNs and assumes 0 instead of them.

We have already mentioned that if the particle is polarizable in the crossed way – electrically (magnetically) by magnetic (electric) field, it must always be polarizable in the "pure" way – electrically by electric and magnetically by magnetic field. Thanks to the linearity of Eq. (2.17), individual contributions from different types of polarizabilities can be calculated separately and we can get the final EELSF as a simple sum of contributions. Dichroism then arises only from the crossed electric-magnetic terms. To study the dichroism, it is thus convenient to calculate and study the dichroic contribution separately, as we will show later in the Sec. [XXX]. We can write this into an equation.

$$\Gamma = \Gamma_{EE} + \Gamma_{EM} + \Gamma_{ME} + \Gamma_{MM}, \quad (2.25)$$

where by the indices EE, EM, ME and MM we denote the component of  $\Gamma$  corresponding to the contribution from polarizability tensors  $\hat{\alpha}_{EE}$ ,  $\hat{\alpha}_{EM}$ ,  $\hat{\alpha}_{ME}$  and  $\hat{\alpha}_{MM}$  respectively. Since  $\hat{\alpha}_{EM} = -\hat{\alpha}_{ME}^T$ ,  $\Gamma_{EM} = \Gamma_{ME}$ . Thus, if we denote the dichroic component of spectrum  $\Gamma_D = 2\Gamma_{EM}$ , we can write

$$\Gamma = \Gamma_{EE} + 2\Gamma_{EM} + \Gamma_{MM} = \Gamma_{EE} + \Gamma_D + \Gamma_{MM}. \quad (2.26)$$

In the following section **Results** we present only  $\Gamma_{EE}$  and  $\Gamma_{EM}$ .

---

<sup>1</sup>The optimization of the computation time was probably the biggest trouble in the implementation process. In the beginning the calculation for approximately 20  $\omega$ -points took several days. A smarter way of libraries usage (including not using some of previously used) was needed and we have managed to get the computation time as low as 4 h–8 h per spectrum.

## 2.3 Results

In the last section of this chapter we present our results in form of spectra. Individual spectra are commented in their captions. Some interesting results are then discussed more thoroughly in the text. We present only the most interesting spectra. Some additional spectra are shown in Appendix A.

There are two sets of spectra. Spectra for electro-electric polarizability and spectra for electro-magnetic polarizability. As we explained above, the presented spectra are only  $\Gamma_{EE}$  and  $\Gamma_{EM}$  contributions.  $\Gamma_{ME}$  would be exactly same as  $\Gamma_{EM}$ , as we have mentioned and  $\Gamma_{MM}$  would have the same shape as  $\Gamma_{EE}$  but would be differently scaled. We do not include the "full" spectra since they would not give any new information and they would look (at first and also second glance) the same as "pure" electro-electric spectra). We are studying the spectra only semi-quantitatively. They are consistent between each other but not properly scaled in absolute value and are featured in arbitrary units (arb. u.). Thus we can compare the values between the spectra in relative measures. When comparing the dichroic spectra to the electro-electric spectra, one needs to have in mind that the scaling between them should reflect the real scaling between electro-electric and cross polarizabilities in the real specimen. In our calculation we have assumed polarizabilities of the same magnitude for crossed and electro-electric polarizabilities in the form of diagonal tensor with equal elements (effectively scalar polarizability of a metal sphere).

In the following figures we mostly hold following conventions. 1) The color of line encodes the information about the initial topological charge  $l_i$  and its change to the final topological charge  $l_f$ . 2) The "density" (dashes, or dots) of the line is lower as the specimen is further away from the center of the vortex.

**Dichroism intensity.** In the descriptions of dichroic spectra we will use the term "dichroic intensity" or "intensity of dichroism". By these terms we mean the relative intensity of dichroic spectrum extrema in comparison to other dichroic spectra or to the non-dichroic (main, electro-electric) signal. An important aspect of this term as we use it is that dichroism intensity "has sign". It is not important what the actual sign is, however, it is important when the profile of dichroic spectrum flips over the zero and changes sign. Meaning, as we will explain later, that instead of "right hand" vortex, the particle now "feels" the vortex as if it was "left hand" and vice versa. If we say that the dichroic intensity is lower, we mean that the extreme values of the spectrum are smaller in absolute value.

In the Fig. 2.2 we can see standard (non-dichroic) EELSFs.

No dichroic response on fig. 2.7: This is happening probably due to a combination of reasons including: 1) The change of the topological charge is symmetric. 2) There is zero probability density of both vortices in the middle. Overall the symmetry of the problem hasn't been broken sufficiently to produce dichroic response.

The most important of our results is that the dependence of dichroism intensity on the position of the specimen relative to the center of vortex is not trivial. See Figs. 2.7 and 2.8. To gain an intuitive understanding of what is happening, take a look at Fig. 2.9. As we move the specimen away from the center of the vortex, the dichroic intensity first gradually increases as we move away from the center of vortex, where it was (due to the symmetry of the problem) zero. From the maximum as we go further away from the center, the dichroic intensity goes again to zero and even flips over to negative values. Again we reach an extremum and then the dichroic response weakens again. This essential means that the vortex probing the particle can see it in completely opposite (in the sense of right- vs. left-hand) manner. The proper knowledge about targeting is thus essential to make any

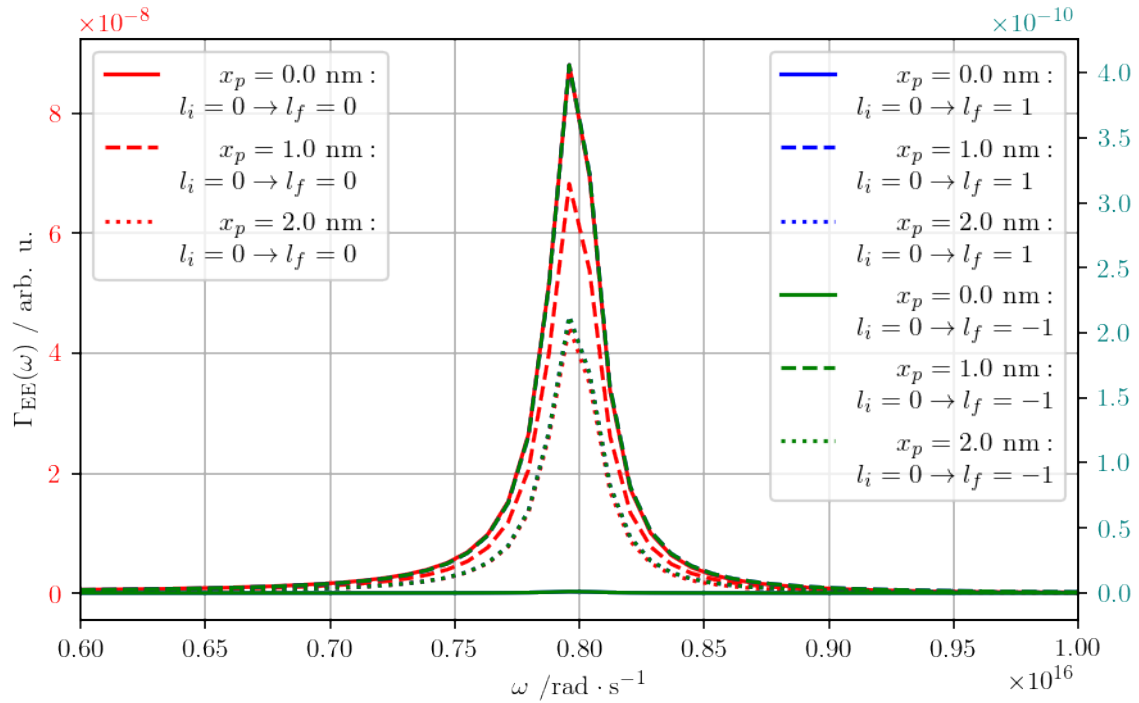


Figure 2.2: Comparison of electro-electric EELS spectra when the initial topological charge  $l_i = 0$  does not change (red) vs changes to the final state  $l_f = 1$  (blue) or  $l_f = -1$  (green). Note that the blue and green spectra are differently scaled (on the right) than red spectra and their magnitude is around two orders of magnitude higher. Green and Blue spectra for  $x_p = 0$  are even another two orders of magnitude lower (so they look as straight lines on first glance). All blue lines are hidden under corresponding green.

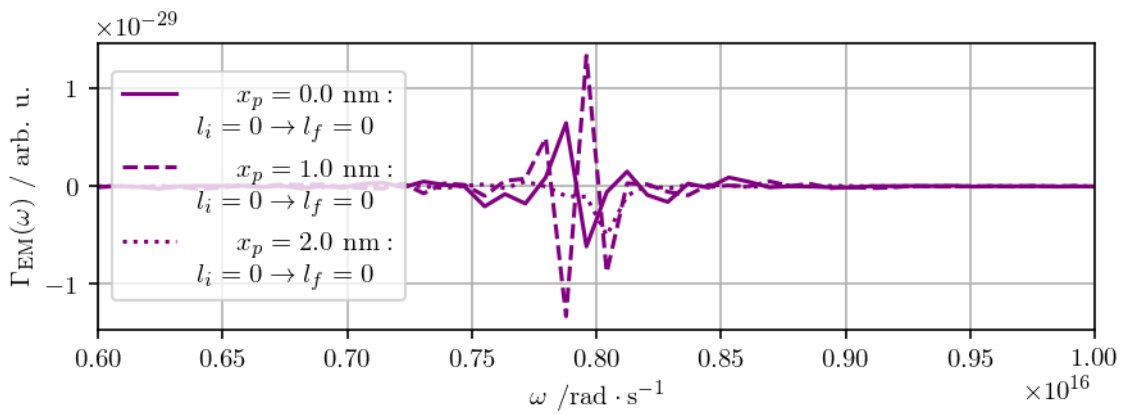


Figure 2.3: (Non)dichroic spectra for non-changing zero topological charge. The symmetry has not been broken so there is no dichroic response and we see only numerical noise.

### 2.3. RESULTS

---

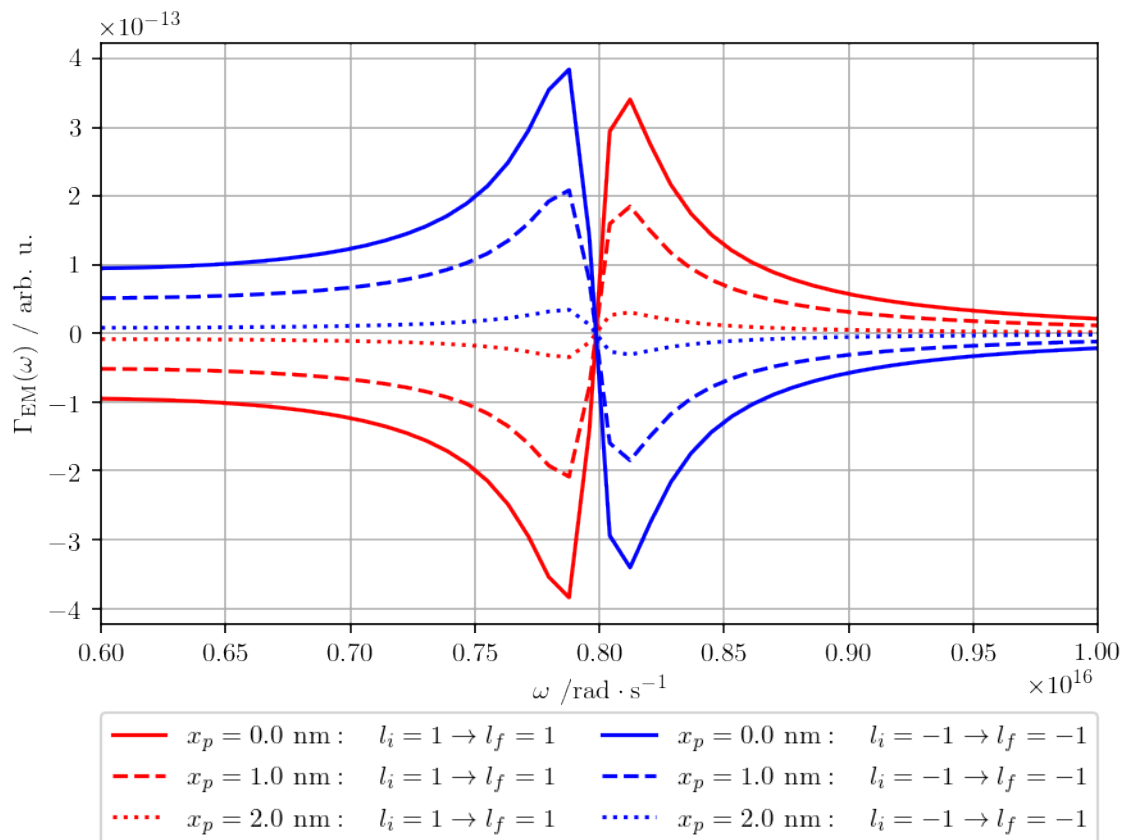


Figure 2.4: Dichroic spectra for non-changing topological charge  $l_i = l_f = \pm 1$ . Here in contrast to Fig. 2.3 the symmetry has been broken and dichroism emerges.

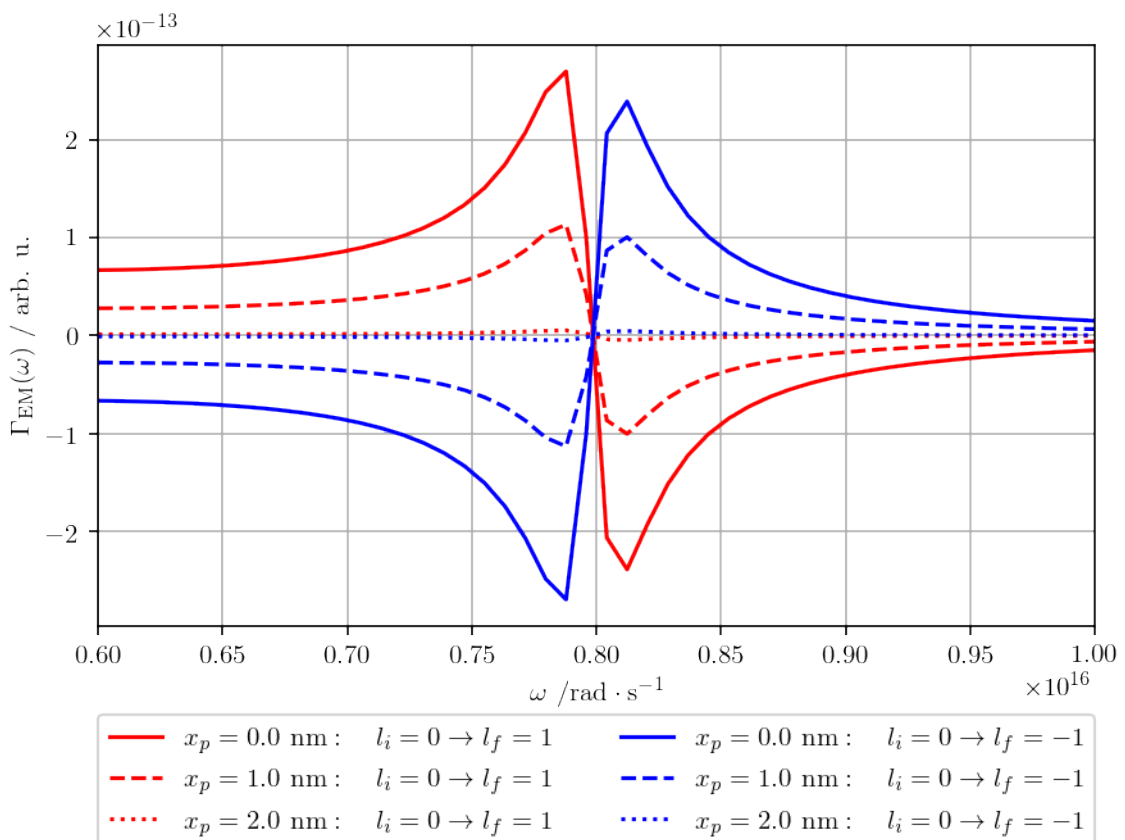


Figure 2.5: The dichroic response to transition of topological charge from 0 to  $\pm 1$  for different distances of specimen from the vortex center.

## 2.3. RESULTS

---

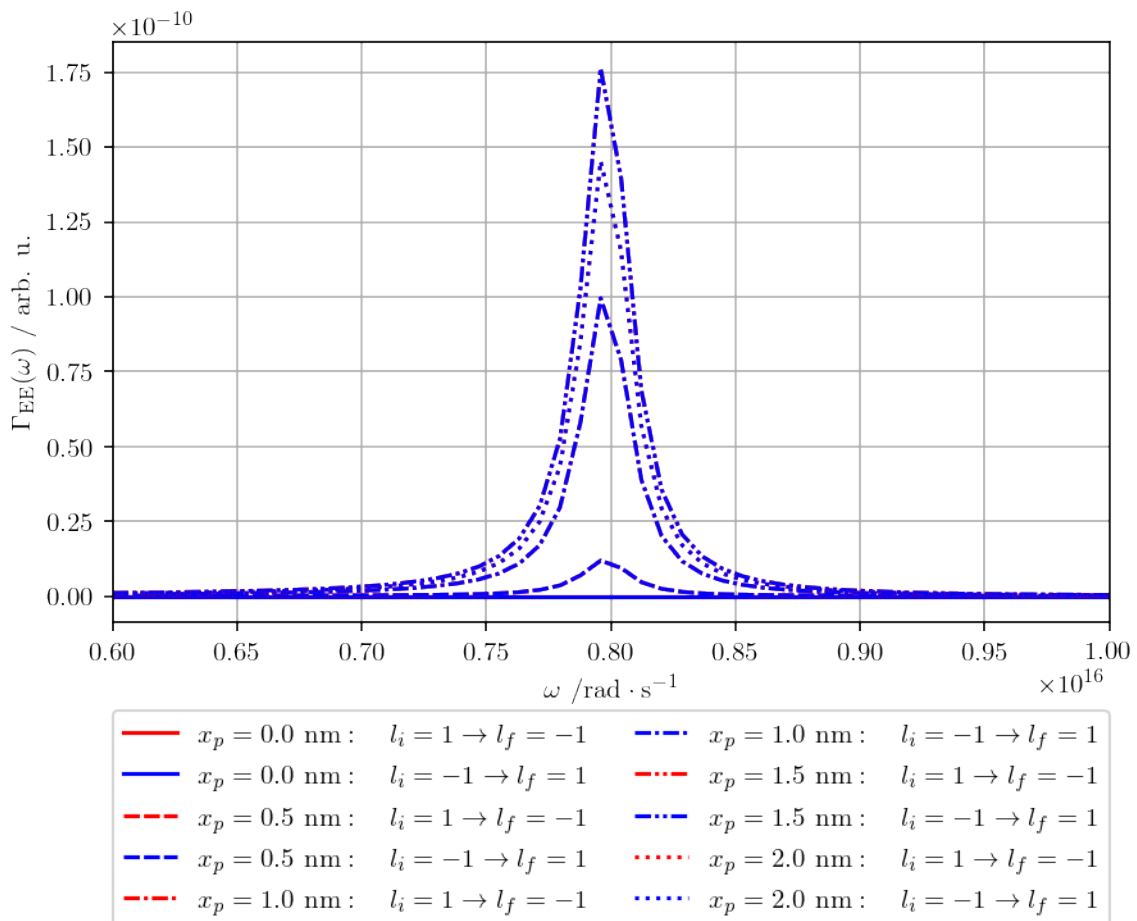


Figure 2.6: Comparison of transitions between topological charges from  $l_i = -1$  to  $l_f = 1$  and vice versa for different positions of specimen. All red lines are hidden under corresponding blue.

conclusions about the specimen and ideally the measurement in this setup with point-like particle shall be performed multiple times so that the vortex is aimed at different spots (with different distances between vortex center and the specimen) around the particle.

The zero topological charge  $l = 0$  is privileged over others. Since the wave function of a vortex is non-zero only in this case. There is then no phase singularity and the problem is way more symmetric. This can lead to the disappearance of dichroism. Interesting things happen also when comparing spectra with topological charge transition symmetric around zero (i. e. from  $+l$  to  $-l$  or vice versa). In this case, the system can be sufficiently symmetric too and the dichroism also does not show.

All in all we can conclude that the problematics of dichroic response to a polarizable point-like particle is multi-factorial and it is hard to formulate some general truths. There are (at least but not only) the initial topological charge magnitude and sign, the change of the topological charge (with respect to its magnitude), and the distance between the center of vortex and the specimen at play. It is possible to gain some intuition but a model should be made for every considered scenario.

## 2.3. RESULTS

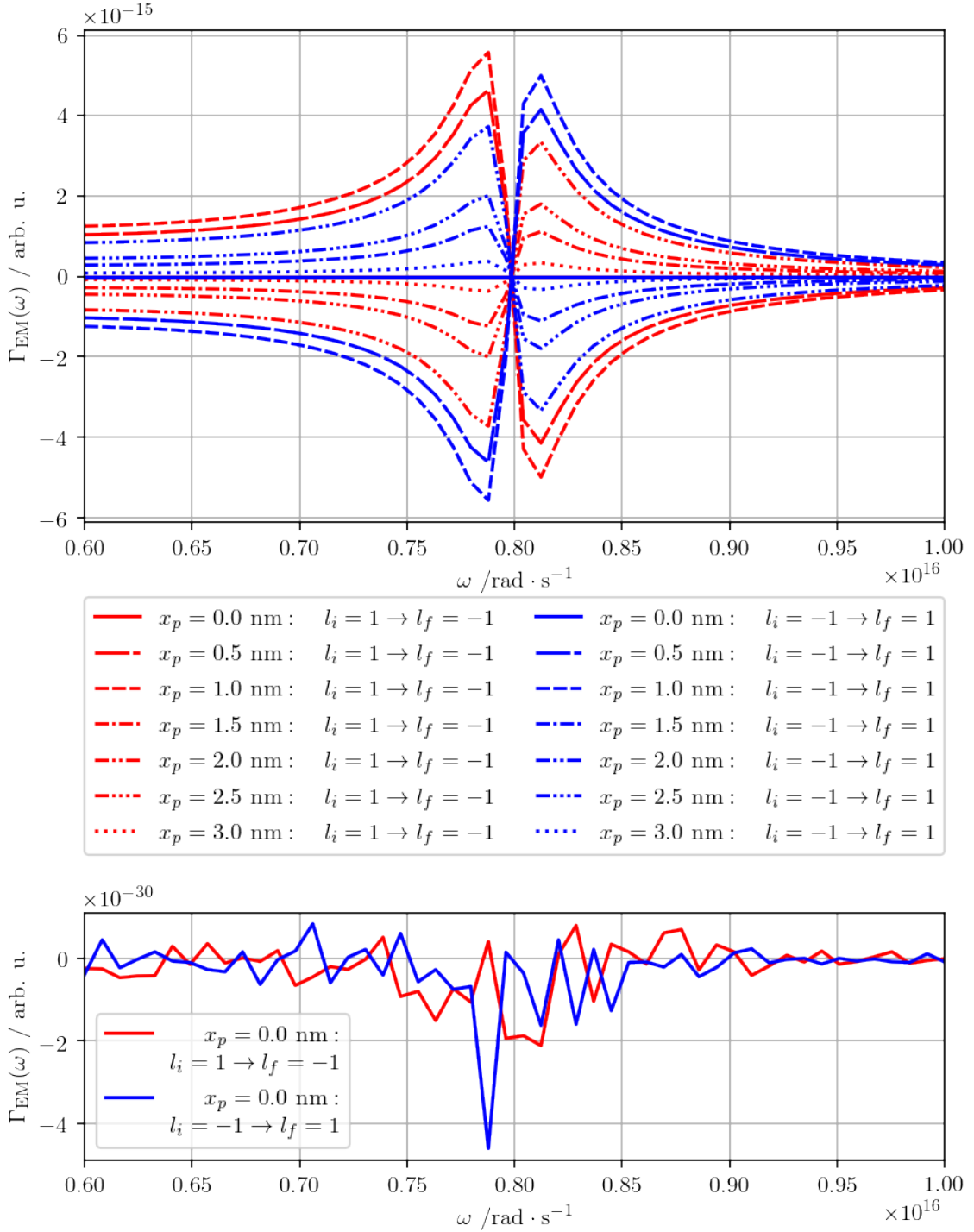


Figure 2.7: Dichroic spectra for the transfer of topological charge between +1 and -1 in both directions for different specimen positions. This figure has the highest information density. First phenomenon we can observe is the opposition of dichroic intensities for opposite topological charge transitions (compare red curves with blue). Secondly we can see (as is zoomed in the lower subplot) that when the specimen is in the center of the vortex, there is no response (and the computed numbers are only numerical noise). Finally we can notice that the dependence of dichroic intensity on the position of the specimen is non-trivial, it even flips over zero (note that in one quadrant there are both red and blue lines). This means that in EELS spectrum, the specimen "looks" as "right-hand" for some distances and "left-hand" for others. See Figs. 2.8 and 2.9 for further detail.

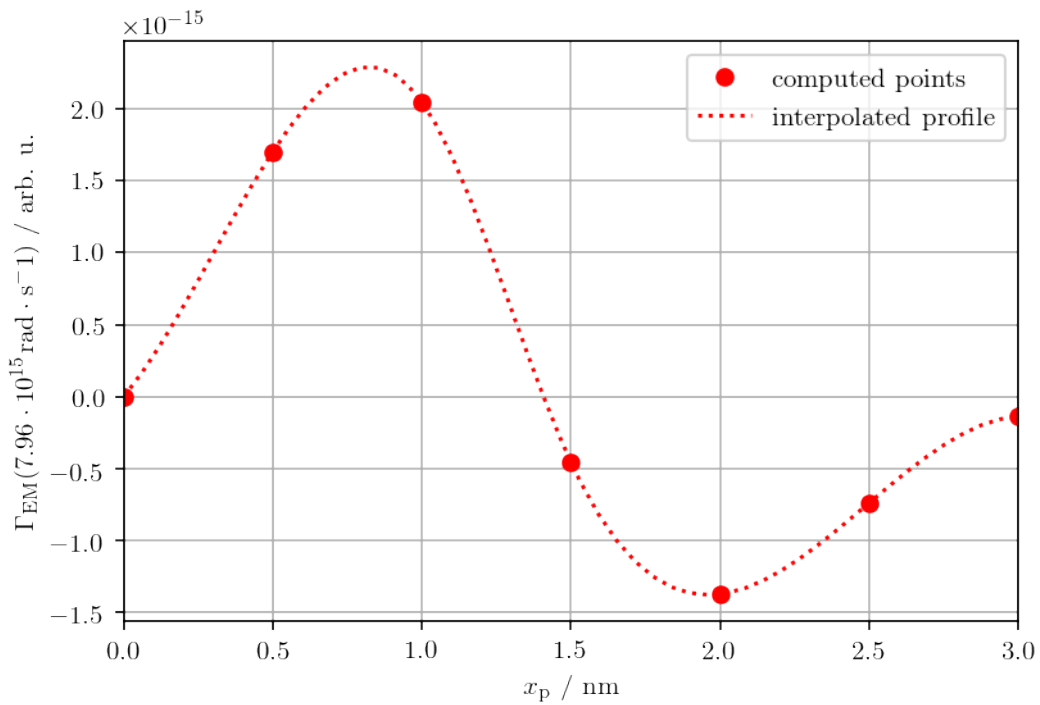


Figure 2.8: The dependence of dichroic response intensity on the position of specimen  $x_p$ . To interpolate the profile a quadratic spline was used, that means the interpolated profile should be viewed critically. In general however, the overall trend should be respected.

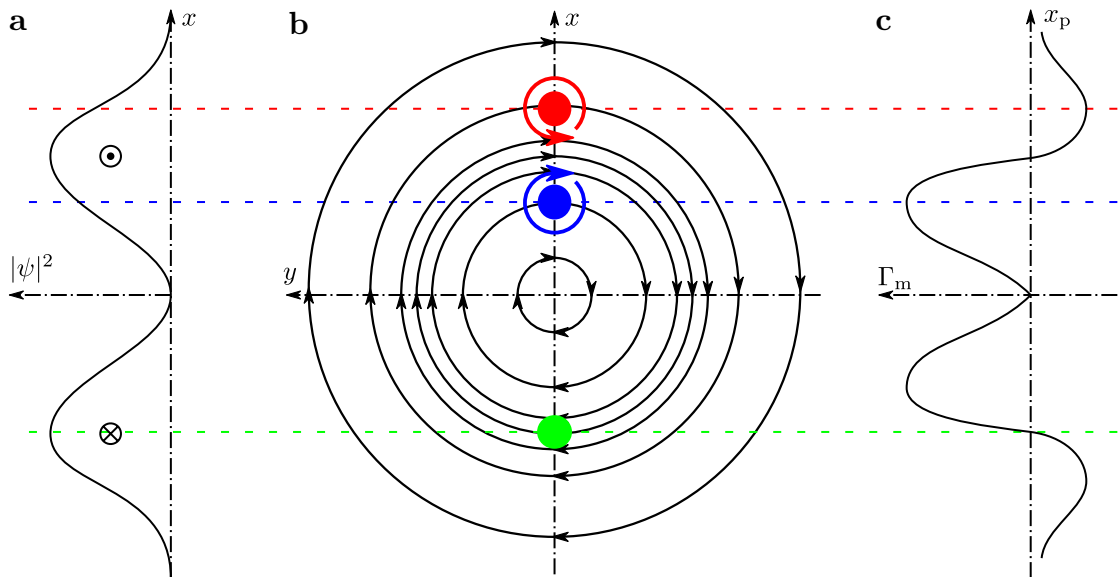


Figure 2.9: Intuition for dependence of response intensity on position of the specimen. a) Probability density of vortex. b) Scheme of vortex circulating around its center. Specimens (in color "feel" the vorticity of the vortex differently depending on their position relative to the main maximum of probability density and can be "spun" in both clockwise and anticlockwise direction. c) Relative intensity of dichroic response dependent on the position of specimen.

# Chapter 3

## Numerical Model

In the last chapter of this thesis we present a model for EELS of VEB interacting with 3D chiral metallic particle. The proposed experiment is very similar to the previous one stated in Ch. 2. The only (although major) difference is that the specimen is not a point-like polarizable particle which can be moved in the beam's profile, but a simple chiral 3D nanostructure consisting of two metallic nanorods (see Fig. 3.1). Due to the complexity of the problem gained by introduction of specific geometry, we have to abandon (semi)analytical methods and approach the problem numerically.

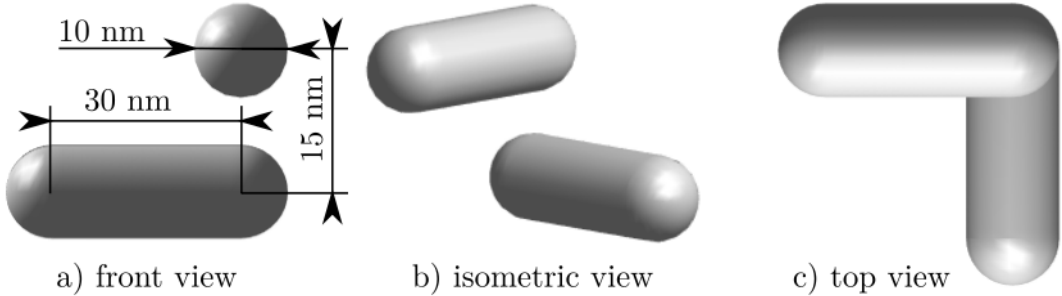


Figure 3.1: Probed chiral nano-structure consisting of two silver rods perpendicular to each other and vertically shifted in respect to each other. Note that mirror image of this structure is incongruent to the original.

As we have previously discussed, electron impinging on a metallic nanostructure is able to excite plasmonic modes. Plasmons quasiparticles emerging from solving Hamiltonian of electron gas in metal and can be understood as collective excitations of charge in the material. They are of two flavours. The first flavour is bulk plasmons which can be neglected in our calculations [26]. The second type of plasmons are surface plasmons. These form on a metal-dielectric interface and the oscillations of the charge are bound to the surface of the metal. Further we refer to surface plasmons only as plasmons. When the material is constrained in all three dimensions, particle plasmons emerge. The excitation then takes the form of a standing wave (i.e. is decomposed in stationary modes). Properties of such oscillations depend heavily on the geometry of the particle in which plasmons are created. If multiple particles are present, plasmons on their surfaces often couple together. Plasmons have evanescent field of high intensity near the surface of the particle (especially around sharp edges). This field can be used to strengthen response in optical systems (e.g. in photovoltaics or scanning near field optical microscope (SNOM)) by concentrating the field in volume. [10]

As was briefly explained, plasmons are an important phenomenon applicable in wide variety of technologies essential for everyday life in 21<sup>st</sup> century. They are often studied in STEM (TEM), particularly with EELS. The usage of VEBs instead of standard beams with zero OAM, which we model, opens new degree of freedom in plasmon analysis. That will, hopefully, lead to deeper understanding of plasmon behaviour on plasmonic structures, particularly chiral ones, which are expected to yield dichroic signal when probed by electron beams carrying non-zero OAM.

### 3.1 Boundary Element Method

In this section we mostly take over the concepts from [10]. To model plasmons one has to find plasmonic modes by solving Maxwell's equations. One of methods which can be used to solve differential equations numerically is Boundary Element Method. Simply stated, in BEM all interfaces (boundaries) are discretised and Maxwell's equations are numerically solved for stated boundary conditions on each finite face of the boundary. In the boundary conditions, not only the geometry of the problem, but also the dielectric constants of used media are contained.

In our case (for small enough structures, we can introduce quasistatic approximation which leads to solving Laplace's equation

$$\nabla^2 \Phi = 0, \quad (3.1)$$

for the scalar potential  $\Phi$  by assuming zero space charge in all environments. Solution of this equation can be written in general form of

$$\Phi(\mathbf{r}) = \Phi_{\text{ext}}(\mathbf{r}) + \oint_{\partial V} d^2 \mathbf{s} G(\mathbf{r}, \mathbf{s}) \sigma(\mathbf{s}) \quad (3.2)$$

for any point in space  $\mathbf{r}$ , where to the external potential  $\Phi_{\text{ext}}(\mathbf{r})$  we add the contribution from the charge distributed on the surface of particle  $\partial V$  by integrating the Green's function  $G$  multiplied by the charge density  $\sigma$  over all the surface elements  $d^2 \mathbf{s}$  of the boundary.

From boundary continuity conditions for fields (i.e. from Maxwell's equations) and charge density one can derive a boundary integral equation of form

$$\Lambda \sigma(\mathbf{s}) + \oint_{\partial V} d^2 \mathbf{s}' \partial_{\mathbf{n}} [G(\mathbf{s}, \mathbf{s}')] \sigma(\mathbf{s}') = -\partial_{\mathbf{n}} \Phi_{\text{ext}}(\mathbf{s}), \quad (3.3)$$

where  $\partial_{\mathbf{n}}$  denotes the derivative along the outer surface normal direction and for dielectric constants of inner and outer environment,  $\varepsilon_1$  and  $\varepsilon_2$ , respectively,  $\Lambda = 2\pi(\varepsilon_2 + \varepsilon_1)/(\varepsilon_2 - \varepsilon_1)$ . From here, we can already see that after the discretization (integrals taking the form of sums) we get (using ESR)

$$[\Lambda \delta_{ij} + (\partial_{\mathbf{n}} G)_{ij}] \sigma_j = -\partial_{\mathbf{n}} (\Phi_{\text{ext}})_i. \quad (3.4)$$

This is formally a problem of eigenvectors and eigenvalues for charge density. Practically it is a system of (generally dense) linear equations which can be solved through simple matrix inversion. Computers can do that very well and fast nowadays.

There exist many BEM solvers. One of them, widely-used and especially well-equipped for dealing with plasmonic problems including EELS is a toolbox for MATLAB called

MNPBEM (for Metal Nano-Particle Boundary Element Method) [10, 11] which we have used for our computations.

After defining the geometry and material characteristics of the studied system, we can call function `bemstateig` which returns several objects including eigenvectors (of pseudo-charge-density distributions corresponding to each little face of the particle system) and eigenvalues (pseudoenergies which correspond to  $2\pi\lambda$  for vacuum wavelength  $\lambda$ ). Surface pseudocharge density is a density of charge located on the surface of the particle which is not necessarily the same, but produces the same field as the real charge distribution.

## 3.2 Interaction of Electron Beam with the Specimen

From now on, we roughly follow [26]. As the electron passes in the vicinity of the specimen, it interacts with every charge in the space around. When plasmonic mode is excited in the particle, the charge is distributed inhomogeneously on the surface of the particle and a field (in quasistatic approximation scalar potential) is created. The Hamiltonian of electron-field interaction can be written as an integral over the interaction volume (or in our case the surface of the particle) with charge density  $\rho$

$$\hat{\mathbf{H}} = - \oint d^3\mathbf{r}' e \frac{\rho(\mathbf{r}')}{|\mathbf{r} - \mathbf{r}'|}. \quad (3.5)$$

Assuming weak interaction, one can find using Fermi's golden rule the EELSF for the transition between well-defined initial  $\psi_i$  and range of final  $\psi_f$  states of electron beam by summing over the assumed final states of electron (f) and all plasmonic modes ( $n$ ) of the specimen.

$$\Gamma(E) \propto \sum_{f,n} \left| \iint d^3\mathbf{r} d^3\mathbf{r}' \frac{\psi_f^*(\mathbf{r}) \psi_i(\mathbf{r}')}{|\mathbf{r} - \mathbf{r}'|} \langle n | \rho(\mathbf{r}') | 0 \rangle \right|^2 \delta(E_f - E_i - E), \quad (3.6)$$

where  $|n\rangle$  and  $|0\rangle$  are the  $n^{\text{th}}$  and ground plasmonic states of the particle, respectively,  $E_f$  and  $E_0$  are the eigenenergies of the  $n^{\text{th}}$  and ground plasmonic states, respectively and  $E$  is the transferred energy.

It is further possible to rewrite this term as

$$\Gamma(E) \propto \sum_f \iint d^3\mathbf{r} d^3\mathbf{r}' \psi_f(\mathbf{r}) \psi_i^*(\mathbf{r}) \text{Im}[-W(\mathbf{r}, \mathbf{r}', E)] \psi_f^*(\mathbf{r}') \psi_i(\mathbf{r}') \delta(E_f - E_i - E), \quad (3.7)$$

where

$$W(\mathbf{r}, \mathbf{r}', E) = \sum_n g_n(E) \Phi_n(\mathbf{r}) \Phi_n^*(\mathbf{r}') \quad (3.8)$$

is the screened interaction between an electron in  $\mathbf{r}$  and in  $\mathbf{r}'$ . It is calculated from the  $n^{\text{th}}$  plasmon eigenpotential  $\Phi_n$  corresponding to the eigenvector of charge density. The factor

$$g_n(E) = \frac{-2}{\varepsilon(1 + \lambda_n) + (1 - \lambda_n)} \quad (3.9)$$

is called spectral function (i.e. the weight function) of  $n^{\text{th}}$  plasmonic mode. Presented form is valid assuming the unit relative permittivity of the environment surrounding the particle of which relative permittivity is  $\varepsilon$ . In the expression we use the eigen-wave-lengths  $\lambda_n$  of  $n^{\text{th}}$  plasmonic mode (these are the results from BEM solution). [7]

In the non-recoil approximation (meaning that the  $z$ -perpendicular wave vector is negligible in comparison to the projection of wave vector to  $z$  axis, which is well fulfilled in our case with VEBs) the last expression for EELS (3.7) can be significantly simplified for particular (vortex) electron state transition  $\psi_i \rightarrow \psi_f$  to the form

$$\Gamma_{i \rightarrow f}(E) \propto \sum_n \text{Im}[-g_n(E)] \left| \iint dx dy \psi_f(x, y) \Phi_n(x, y, \omega) \psi_i^*(x, y) \right|^2, \quad (3.10)$$

where  $\Phi_n(x, y, \omega)$  is the  $z$ -Fourier transform of the  $n^{\text{th}}$  plasmon eigenpotential which emerged from the integration along  $z$ . It can be calculated by integrating over all the charge densities  $\sigma$  on all of boundary surfaces  $S$  as

$$\Phi_n(\mathbf{r}_\perp, \omega) = 2 \oint_S d^2\mathbf{s} \sigma_n(\mathbf{s}) e^{-i\omega s_z/v} K_0 \left( \frac{\omega |\mathbf{r}_\perp - \mathbf{s}_\perp|}{v} \right), \quad (3.11)$$

where transferred energy  $E = \hbar\omega$ ,  $v$  is the speed of electron and in the argument of modified Bessel function of second kind of order 0,  $K_0$ , we denote the  $z$ -perpendicular projections by symbol  $\perp$ . [7]

In our calculations we assume the same as in previous section that the initial and final states of electron beam are VEBs of form (1.19).

### 3.3 Implementation and Choice of Computation Parameters

To implement the model for EELSF of VEB interacting with chiral structure shown in Fig. 3.1 We first needed to find the eigenstates of plasmons in this particle. For this purpose a toolbox MNPBEM for Matlab was used [10, 11]. After the extraction of charge eigendensities (eigenvectors) and eigenenergies (eigenvalues) together with positions and areas of modelled particle's faces, we have moved to python.

Libraries numpy, scipy and matplotlib were used in the computation scripts. The first thing to do was to calculate the  $g$ -factors according to Exp. (3.9) for range of possible frequencies  $\omega$ . In Fig. 3.2 we have plotted  $g$ -factors over frequency domain for the first 15 plasmonic modes. We can easily see in the graph that if we restrict our studied interval of frequencies to  $3 \cdot 10^{15} \text{ rad} \cdot \text{s}^{-1}$ – $5.5 \cdot 10^{15} \text{ rad} \cdot \text{s}^{-1}$ , we can study only the effect of the first two plasmonic modes since the influence of higher modes is negligible. The two  $g$ -factors over constrained interval of frequencies are plotted in Fig. 3.3.

After the  $g$ -factors were calculated, the  $z$ -Fourier transforms of potentials  $\Phi_n(\omega)$  produced by the  $n^{\text{th}}$  plasmonic mode driven on frequency  $\omega$  were calculated from the Exp. (3.11).

### 3.4 Results

### 3.4. RESULTS

---

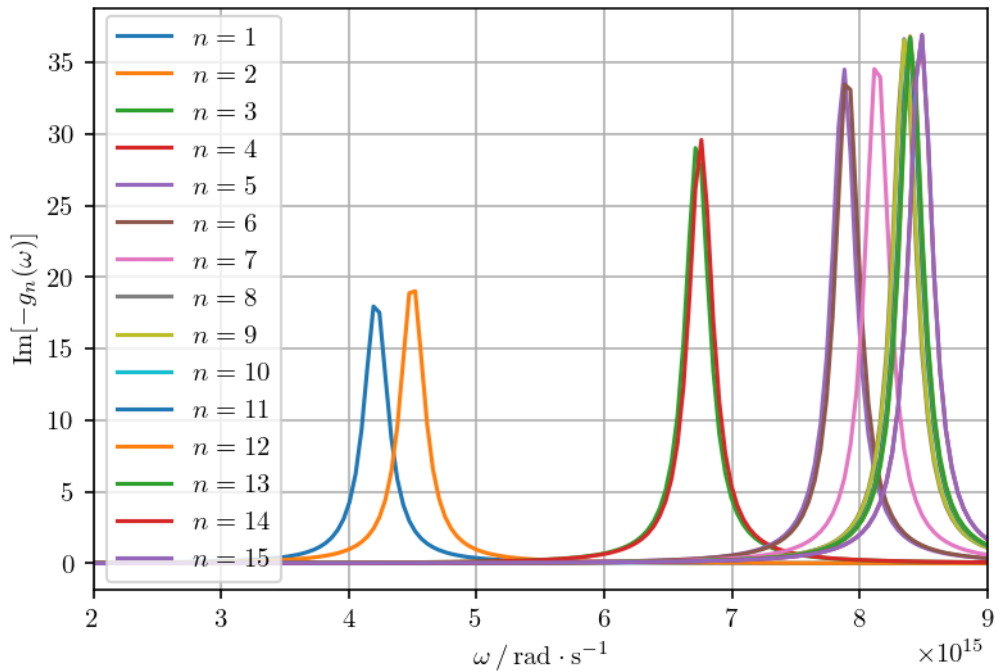


Figure 3.2: Spectral function  $g$  (its negative imaginary part) profiles over frequency  $\omega$  domain for first 15 plasmonic modes  $n$ .

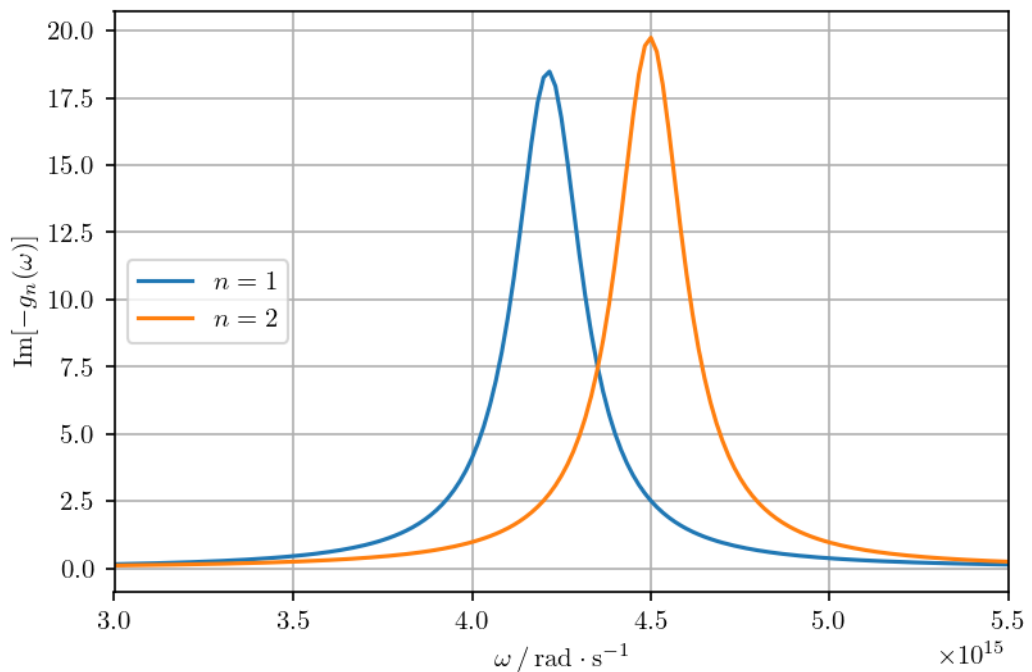


Figure 3.3: Spectral function  $g$  (its negative imaginary part) profiles over frequency  $\omega$  interval constrained so that only the first two plasmonic modes  $n$  are significant.

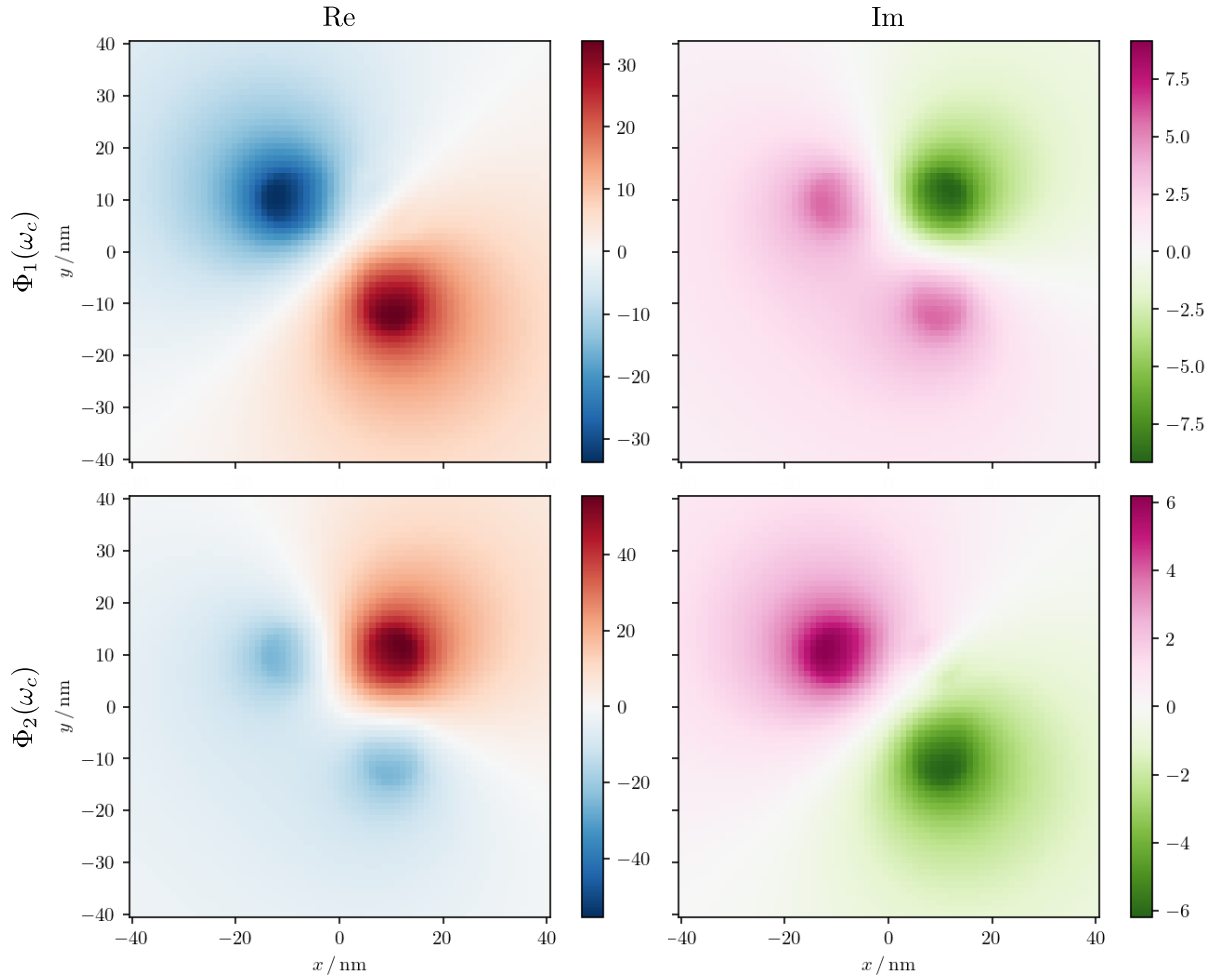


Figure 3.4:  $z$ -Fourier transform of potentials produced by first two plasmonic modes driven by frequency  $\omega_c = 3.3 \cdot 10^{15} \text{ rad} \cdot \text{s}^{-1}$ . In the left columns we can see real parts and in the right imaginary parts of potentials. From the profiles of potentials (and the fact that their resonant frequencies (eigenenergies) are near each other (see Figs. 3.2 and 3.3) we can interpret them as the bonding ( $n = 1$ ) and anti-bonding ( $n = 2$ ) modes of the two nanorods.

# Summary



## Appendix A

### Some More Calculated Spectra

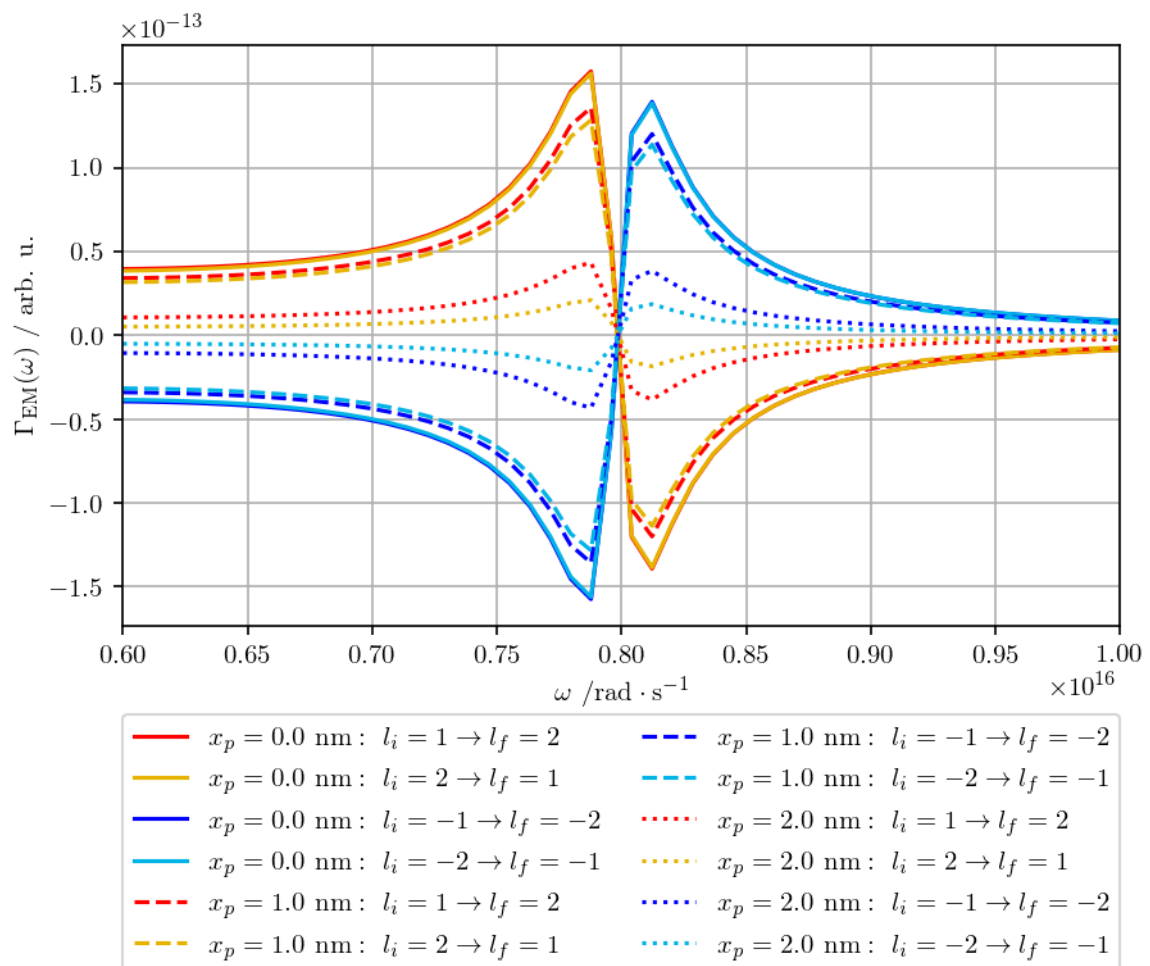


Figure A.1: Caption

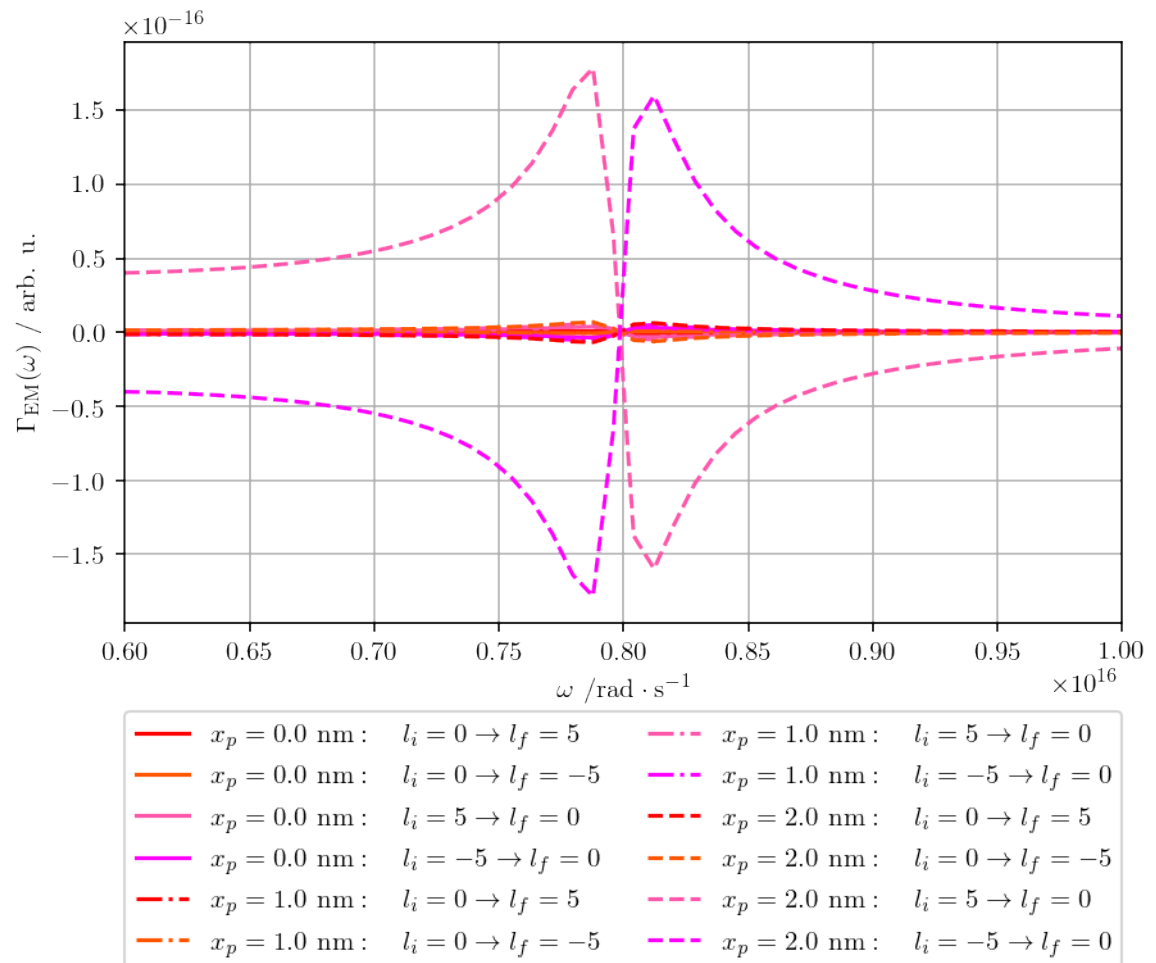


Figure A.2: Caption

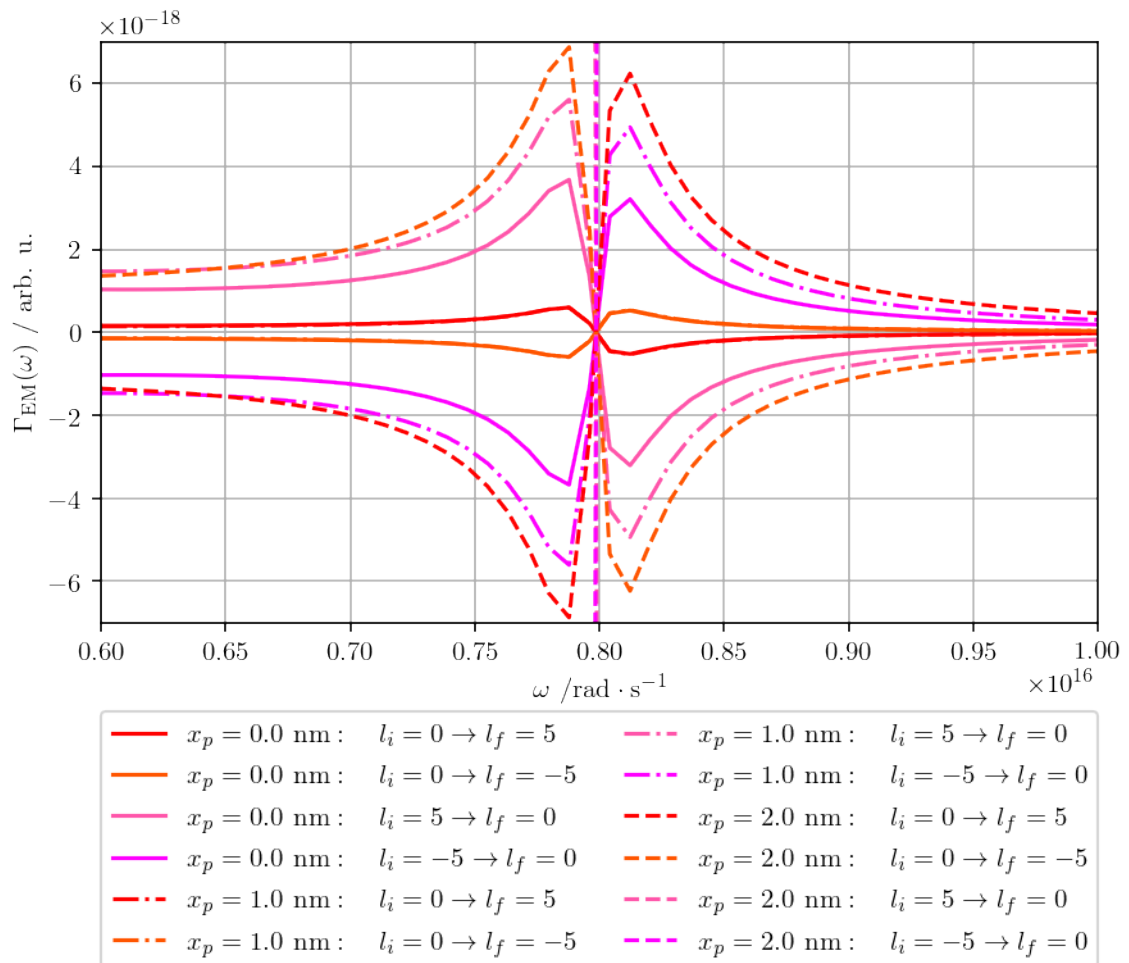


Figure A.3: Caption

# Appendix B

## Notes on Maths

### B.1 Square Root Approximation

Assume an expression in a form of

$$\sqrt{1+x}, \quad (\text{B.1})$$

where  $x \ll 1$ . By expanding it with Maclaurin series (Taylor series with the center in 0) we can write

$$\sqrt{1+x} = 1 + \frac{1}{2}x + O(x^2). \quad (\text{B.2})$$

If  $x$  is sufficiently small, we can neglect  $O(x^2)$  and write

$$\sqrt{1+x} \approx 1 + \frac{1}{2}x. \quad (\text{B.3})$$

This approximation rule is widely used in paraxial approximations.

### B.2 Cylindrical coordinates

It might be convenient to describe a problem in cylindrical coordinates rather than in Cartesian when there exists some kind of axial symmetry. Let  $z$  be the direction of the axis of symmetry. Then any vector  $\mathbf{r}$  described by Cartesian coordinates  $x$ ,  $y$  and  $z$  can be described by new set of coordinates: radius  $r$  and angle of deviation from  $x$  axis denoted  $\phi$  together with formerly used  $z$  (see Fig. B.1).

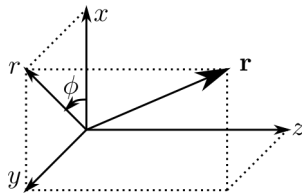


Figure B.1: Cylindrical coordinates.

The transformation equations are

$$\begin{aligned} x &= r \cos \phi, \\ y &= r \sin \phi, \quad \text{and} \\ z &= z. \end{aligned} \quad (\text{B.4})$$

The inverse transformation rules are

$$\begin{aligned} r &= \sqrt{x^2 + y^2}, \\ \phi &= \arctan2(y, x), \quad \text{and} \\ z &= z. \end{aligned} \tag{B.5}$$

### B.3 Evaluation of integral (1.16) using Jacobi–Anger expansion

We will now focus on an integral of form

$$I = \int_0^{2\pi} d\phi e^{il\phi} e^{iQ \cos(\phi - \theta)}. \tag{B.6}$$

From [25] we get Jacobi–Anger expansion:

$$e^{iQ \cos(\phi)} = \sum_{n=-\infty}^{\infty} i^n J_n(Q) e^{in\phi} \tag{B.7}$$

Substituting Eq. (B.7) into the Eq. (B.6) and rearranging we get

$$I = \sum_{n=-\infty}^{\infty} i^n e^{-in\theta} J_n(Q) \int_0^{2\pi} d\phi e^{il\phi} e^{in\phi}. \tag{B.8}$$

From residue theorem we can find (for  $t \in \langle 0, 2\pi \rangle$ ), that

$$\int_0^{2\pi} d\phi e^{il\phi} e^{in\phi} = \oint_{z=e^{it}} dz^{n+l-1}(-i) = \delta_{l,-n}. \tag{B.9}$$

This leads to the final result below. In the last step we have used [8, Eq. 10.4.1].

$$I = 2\pi i^{-l} J_{-l}(Q) e^{il\theta} = 2\pi i^l J_l(Q) e^{il\theta}. \tag{B.10}$$

# List of Figures

1.1	Scheme for the construction of the diffraction integral. . . . .	6
1.2	Measurement and Preparation of VEBs, Uchida and Verbeeck. . . . .	9
1.3	An example of VEBs prepared by ideal phase plates for two different topological charges (a, b) and using square-matrix of einzel lenses (c, d, e) retarding the wave function by factor of phase in first row. Note that the wave function produced in cases d and e is already quite near the ideal state (a). . . . .	10
1.4	Another example of VEBs prepared by round einzel lenses arranged around circle. Note that for $N = 4$ the square symmetry manifests significantly. For higher numbers of lenses, however, produced vortex are getting better fast. .	10
1.5	Scheme of modelled experiment . . . . .	11
2.1	Diagram of the interaction of an electron with the specimen. . . . .	22
2.2	Comparison of electro-electric EELS spectra when the initial topological charge $l_i = 0$ does not change (red) vs changes to the final state $l_f = 1$ (blue) or $l_f = 1$ (green). Note that the blue and green spectra are differently scaled (on the right) than red spectra and their magnitude is around two orders of magnitude higher. Green and Blue spectra for $x_p = 0$ are even another two orders of magnitude lower (so they look as straight lines on first glance). All blue lines are hidden under corresponding green. . . . .	26
2.3	(Non)dichroic spectra for non-changing zero topological charge. . . . .	26
2.4	Dichroic spectra for non-changing topological charge $l_i = l_f = \pm 1$ . . . . .	27
2.5	The dichroic response to transition of topological charge from 0 to $\pm 1$ for different distances of specimen from the vortex center. . . . .	28
2.6	Comparison of transitions between topological charges from $l_i = -1$ to $l_f = 1$ and vice versa for different positions of specimen. All red lines are hidden under corresponding blue. . . . .	29
2.7	Dichroic spectra for the transition of topological charge between +1 and -1 in both directions for different specimen positions. . . . .	31
2.8	The dependence of dichroic response intensity on the position of specimen. .	32
2.9	Intuition for dependence of dichroic response intensity on position of the specimen. . . . .	32
3.1	Probed chiral nano-structure consisting of two silver rods perpendicular to each other and vertically shifted in respect to each other. Note that mirror image of this structure is incongruent to the original. . . . .	33
3.2	Spectral function $g$ (its negative imaginary part) profiles over frequency $\omega$ domain for first 15 plasmonic modes $n$ . . . . .	37

3.3	Spectral function $g$ (its negative imaginary part) profiles over frequency $\omega$ interval constrained so that only the first two plasmonic modes $n$ are significant.	37
3.4	$z$ -Fourier transform of potentials produced by first two plasmonic modes drived by frequency $\omega_c = 3.3 \cdot 10^{15} \text{ rad} \cdot \text{s}^{-1}$ .	38
A.1	Caption	42
A.2	Caption	43
A.3	Caption	44
B.1	Cylindrical coordinates.	45

# List of Symbols

---

## APPENDIX B. LIST OF SYMBOLS

# List of Abbreviations

**1D, 2D, 3D, 4D,...** one-, two- three- four-dimension(al)

**CL** CathodoLuminiscence,

**BEM** Boundary Element Method

**EELS** Electron Energy Loss Spectroscopy,

**EELSF** Electron Energy Loss Spectral Function,

**EM** Electromagnetic

**LDOS** local density of optical states

**OAM** Orbital Angular Momentum,

**PPP** Programmable Phase Plate

**SEM** Scanning Electron Microscope

**STEM** Scanning Transmission Electron Microscopy

**TEM** Transmission Electron Microscopy

**VE** Vortex Electron, Electron Vortex, can be interchanged with VEB

**VEB** Vortex Electron Beam

---

APPENDIX B. LIST OF ABBREVIATIONS

# References

- [1] F. J. García De Abajo. “Optical excitations in electron microscopy.” In: *Reviews of Modern Physics* 82 (1 Feb. 2010), pp. 209–275. ISSN: 00346861. DOI: 10.1103/RevModPhys.82.209.
- [2] G. Anzolin et al. “Method to measure off-axis displacements based on the analysis of the intensity distribution of a vortex beam.” In: *Physical Review A - Atomic, Molecular, and Optical Physics* 79 (3 Mar. 2009). Preparation of vortex electron beam from plane wave. ISSN: 10502947. DOI: 10.1103/PhysRevA.79.033845.
- [3] A. Asenjo-Garcia and F. J. García De Abajo. “Dichroism in the interaction between vortex electron beams, plasmons, and molecules.” In: *Physical Review Letters* 113 (6 Aug. 2014). ISSN: 10797114. DOI: 10.1103/PhysRevLett.113.066102.
- [4] Richard A. Beth. “Direct Detection of the Angular Momentum of Light.” In: *Phys. Rev.* 48 (5 Sept. 1935), pp. 471–471. DOI: 10.1103/PhysRev.48.471. URL: <https://link.aps.org/doi/10.1103/PhysRev.48.471>.
- [5] K. Y. Bliokh et al. *Theory and applications of free-electron vortex states*. May 2017. DOI: 10.1016/j.physrep.2017.05.006.
- [6] Michel Bosman et al. “Mapping surface plasmons at the nanometre scale with an electron beam.” In: *Nanotechnology* 18.16 (Mar. 2007), p. 165505. DOI: 10.1088/0957-4484/18/16/165505. URL: <https://doi.org/10.1088/0957-4484/18/16/165505>.
- [7] Guillaume Boudarham and Mathieu Kociak. “Modal decompositions of the local electromagnetic density of states and spatially resolved electron energy loss probability in terms of geometric modes.” In: *Phys. Rev. B* 85 (24 June 2012), p. 245447. DOI: 10.1103/PhysRevB.85.245447. URL: <https://link.aps.org/doi/10.1103/PhysRevB.85.245447>.
- [8] *NIST Digital Library of Mathematical Functions*. F. W. J. Olver, A. B. Olde Daalhuis, D. W. Lozier, B. I. Schneider, R. F. Boisvert, C. W. Clark, B. R. Miller, B. V. Saunders, H. S. Cohl, and M. A. McClain, eds. URL: <http://dlmf.nist.gov/>.
- [9] F. J. García de Abajo and M. Kociak. “Probing the Photonic Local Density of States with Electron Energy Loss Spectroscopy.” In: *Phys. Rev. Lett.* 100 (10 Mar. 2008), p. 106804. DOI: 10.1103/PhysRevLett.100.106804. URL: <https://link.aps.org/doi/10.1103/PhysRevLett.100.106804>.
- [10] Ulrich Hohenester and Andreas Trügler. “MNPBEM – A Matlab toolbox for the simulation of plasmonic nanoparticles.” In: *Computer Physics Communications* 183.2 (Feb. 2012), pp. 370–381. DOI: 10.1016/j.cpc.2011.09.009. URL: <https://doi.org/10.1016%2Fj.cpc.2011.09.009>.

- 
- [11] Universität Graz Institut für Physik. *MNPBEM*. URL: <https://physik.uni-graz.at/de/mnpbem/> (visited on 05/15/2022).
  - [12] Jiří Komrska. *Difrakce*. 2007. URL: <http://physics.fme.vutbr.cz/~komrska/Difrakce/>.
  - [13] Andrea Konečná et al. *Probing the electromagnetic response of dielectric antennas by vortex electron beams*. 2021. arXiv: 2111.08810 [physics.optics].
  - [14] Yuuki Noguchi et al. “Efficient Measurement of the Orbital-Angular-Momentum Spectrum of an Electron Beam via a Dammann Vortex Grating.” In: *Physical Review Applied* 12 (6 Dec. 2019), p. 064062. ISSN: 23317019. DOI: 10.1103/PhysRevApplied.12.064062.
  - [15] Lukas Novotny and Bert Hecht. *Principles of Nano-Optics*. 2nd ed. Cambridge University Press, 2012. ISBN: 978-1-107-00546-4.
  - [16] Albert Polman, Mathieu Kociak, and F. Javier García de Abajo. “Electron-beam spectroscopy for nanophotonics.” In: *Nature Materials* 18 (11 Nov. 2019), pp. 1158–1171. ISSN: 14764660. DOI: 10.1038/s41563-019-0409-1.
  - [17] Koh Saitoh et al. “Production of electron vortex beams carrying large orbital angular momentum using spiral zone plates.” In: *Journal of Electron Microscopy* 61.3 (Mar. 2012), pp. 171–177. ISSN: 0022-0744. DOI: 10.1093/jmicro/dfs036. eprint: <https://academic.oup.com/jmicro/article-pdf/61/3/171/5854114/dfs036.pdf>. URL: <https://doi.org/10.1093/jmicro/dfs036>.
  - [18] A. H. Tavabi et al. *Generation of electron vortex beams with over 1000 orbital angular momentum quanta using a tuneable electrostatic spiral phase plate*. 2022. DOI: 10.48550/ARXIV.2203.00477. URL: <https://arxiv.org/abs/2203.00477>.
  - [19] Masaya Uchida and Akira Tonomura. “Generation of electron beams carrying orbital angular momentum.” In: *Nature* 464 (7289 Apr. 2010), pp. 737–739. ISSN: 00280836. DOI: 10.1038/nature08904.
  - [20] G. M. Vanacore et al. “Ultrafast generation and control of an electron vortex beam via chiral plasmonic near fields.” In: *Nature Materials* 18 (6 June 2019), pp. 573–579. ISSN: 14764660. DOI: 10.1038/s41563-019-0336-1.
  - [21] J. Verbeeck, H. Tian, and A. Béché. “A new way of producing electron vortex probes for STEM.” In: *Ultramicroscopy* 113 (Feb. 2012), pp. 83–87. ISSN: 03043991. DOI: 10.1016/j.ultramic.2011.10.008.
  - [22] J. Verbeeck, H. Tian, and P. Schattschneider. “Production and application of electron vortex beams.” In: *Nature* 467 (7313 Sept. 2010), pp. 301–304. ISSN: 00280836. DOI: 10.1038/nature09366.
  - [23] Jo Verbeeck, He Tian, and Gustaaf Van Tendeloo. “How to Manipulate Nanoparticles with an Electron Beam?” In: *Advanced Materials* 25 (8 Feb. 2013), pp. 1114–1117. ISSN: 09359648. DOI: 10.1002/adma.201204206. URL: <https://onlinelibrary.wiley.com/doi/10.1002/adma.201204206>.
  - [24] Jo Verbeeck et al. “Demonstration of a  $2 \times 2$  programmable phase plate for electrons.” In: *Ultramicroscopy* 190 (2018), pp. 58–65. ISSN: 0304-3991. DOI: <https://doi.org/10.1016/j.ultramic.2018.03.017>. URL: <https://www.sciencedirect.com/science/article/pii/S0304399117305041>.

## REFERENCES

---

- [25] Eric W. Weisstein. *Jacobi-Anger Expansion. From MathWorld—A Wolfram Web Resource*. Last accesed 6 December 2021. 2021. URL: <https://mathworld.wolfram.com/Jacobi-AngerExpansion.html>.
- [26] Matteo Zanfognini et al. “Orbital Angular Momentum and Energy Loss Characterization of Plasmonic Excitations in Metallic Nanostructures in TEM.” In: *ACS Photonics* 6 (3 Mar. 2019), pp. 620–627. ISSN: 23304022. doi: 10.1021/acsphotonics.9b00131.